Lithos 202–203 (2014) 267–282

Contents lists available at ScienceDirect

Lithos

journal homepage: www.elsevier.com/locate/lithos

Composition and structure of the lithospheric mantle beneath NE Iran: Constraints from mantle xenoliths

Ben-Xun Su [a,b,*], Sun-Lin Chung [c,d,**], Mohammad Hossein Zarrinkoub [e], Kwan-Nang Pang [c], Ling Chen [a], Wei-Qiang Ji [a], Aaron Brewer [f], Ji-Feng Ying [a], Mohammad Mahdi Khatib [e]

[a] State Key Laboratory of Lithospheric Evolution, Institute of Geology and Geophysics, Chinese Academy of Sciences, P.O. Box 9825, Beijing 100029, China
[b] Department of Earth Sciences, University of Hong Kong, Hong Kong, China
[c] Department of Geosciences, National Taiwan University, Taipei, Taiwan
[d] Institute of Earth Sciences, Academia Sinica, Taipei, Taiwan
[e] Department of Geology, University of Birjand, Birjand, Iran
[f] Isotope Laboratory, Department of Earth and Space Sciences, University of Washington, Seattle, WA 98195, USA

ARTICLE INFO

Article history:
Received 4 April 2014
Accepted 3 June 2014
Available online 11 June 2014

Keywords:
Mantle xenolith
Iranian Plateau
Lithospheric mantle
Metasomatism
Partial melting
Tethyan subduction

ABSTRACT

A detailed study on petrology and mineral chemistry of 32 mantle xenoliths has been conducted to decipher the physical and chemical characteristics of the lithosphere beneath NE Iran. Spinel lherzolite, the most abundant xenolith type, is made up of olivine, orthopyroxene, clinopyroxene, and spinel. Clinopyroxenes in the spinel lherzolites display a primitive mantle-like composition, typical of non-cratonic peridotites. Pyroxenite, another major xenolith type, shows equilibrated textures and highly variable compositions including olivine websterite, websterite and clinopyroxenite. These pyroxenites, together with an equigranular dunite, delineate a clear metasomatic trend, characterized by systematic Mg#, Cr#, Al_2O_3, and TiO_2 variations in the constituent minerals, coupled with light rare earth element enrichment and high field strength element depletion in clinopyroxene. The pyroxenites are therefore suggested to have formed by the interaction between garnet-bearing peridotites within the lithospheric mantle and melts from a stagnant slab within the asthenosphere. The lithospheric mantle may have undergone multiple stages of partial melting. The earliest stage, evidenced by the equigranular dunite, resulted in significant NiO depletion in olivine, low Al_2O_3 and TiO_2 coupled with high Mg# and Cr# in clinopyroxene, and high Cr# in spinel. The second stage occurred more widely and gave rise to the large ion lithophile element depletion in clinopyroxenes of all rock types. The extent of melting is lower in the spinel lherzolites than that in the pyroxenites, implying that the partial melting was not caused by decompression and thus most likely related to Tethyan subduction. A third and more recent melting stage, responsible for the spongy texture in some clinopyroxenes, is attributed to the extensional tectonic regime that started in the middle Miocene in the region. Temperature estimates show that both the spinel lherzolites and pyroxenites equilibrated at ~900–1000 °C. Based on our new data and published data we propose the lithospheric structure beneath NE Iran. The xenolith-defined geotherm appears to be hotter than that typical in cratonic and oceanic settings, but colder than that suggested by seismic tomographic modeling for the entire Iranian Plateau. This difference is probably due to the widespread occurrence of pyroxenites within the lithospheric mantle, which we argue could have played a significant role in causing not only the seismic and gravitational anomalies but also late Cenozoic volcanism on the Iranian Plateau.

1. Introduction

The Iranian Plateau was formed through the long-lived convergence between the Arabian and Eurasian plates since the Late Cretaceous with the final closure of the Neo-Tethys ocean (Golonka, 2004; Hatzfeld and Molnar, 2010; Jimenez-Munt et al., 2012). The ongoing continental collision and, more importantly, "post-initial collision" geodynamic processes make this region a younger, or "immature", analogue of the Tibetan Plateau (Chung et al., 2005; Manaman and Shomali, 2010; Ni and Barazangi, 1986). The lithospheric structure beneath the Iranian Plateau remains poorly constrained. Although lithospheric thickening related to the Arabia-Eurasia collision has been a widely accepted interpretation (e.g., Allen et al., 2013; Maggi and Priestley, 2005), geodynamic processes such as lithospheric thinning and delamination (Kay and Mahlburg Kay, 1993) and/or slab detachment (Davies and von Blanckenburg, 1995)

* Correspondence to: B.-X. Su, State Key Laboratory of Lithospheric Evolution, Institute of Geology and Geophysics, Chinese Academy of Sciences, P.O. Box 9825, Beijing 100029, China. Tel.: +86 10 82998514; fax: +86 10 62010846.
** Correspondence to: S.-L. Chung, Department of Geosciences, National Taiwan University, Taipei, Taiwan. Tel.: +886 8369 1242; fax: +886 2363 6095.
E-mail addresses: subenxun@mail.igcas.ac.cn (B.-X. Su), sunlin@ntu.edu.tw (S.-L. Chung).

http://dx.doi.org/10.1016/j.lithos.2014.06.002
0024-4937/

have been proposed. Nevertheless, studies have reported the existence of geophysical anomalies that are spatially correlated with the distribution of major faults and/or mantle-derived volcanism in Iran (Allen et al., 2013; Kaviani et al., 2009; Maggi and Priestley, 2005; Omrani et al., 2008; Paul et al., 2010), and the latter is potentially capable of indicating the lithospheric composition and structure.

The petrogenesis of widespread volcanic rocks in the Iranian Plateau, active through the Eocene to Quaternary (Fig. 1a), is still however, controversial (Allen et al., 2013; Asiabanha and Foden, 2012; Chiu et al., 2013; Pang et al., 2012, 2013a,b; Verdel et al., 2011). The potassic–ultrapotassic volcanic rocks from NW Iran have been ascribed to small-degree melting of the metasomatized lithospheric mantle (e.g., Pang et al., 2013a) as have more sodic small-volume basaltic volcanic rocks from the same region (Allen et al., 2013; Kheirkhah et al., 2013). These NW Iranian rocks have been variably attributed to slab break-off (Alaminia et al., 2013; Allen et al., 2013), lithospheric extension associated with asthenospheric upwelling (McKenzie and Bickle, 1988; Pang et al., 2013a), and melting at the base of the lithosphere or compressional melting caused by breakdown of hydrous phases in the mantle lithosphere due to ongoing collision (Allen et al., 2013; Kheirkhah et al., 2013). The geochemical variation displayed by the Miocene to Quaternary intra-plate basalts in eastern Iran has also led to a variety of postulated source regions and melting regimes. Some studies suggest that these basalts were derived from the garnet-spinel peridotite transition zone (Saadat and Stern, 2012) by decompression melting (Priestley et al., 2012), whereas others have argued that these basalts most likely have asthenospheric origin with low degrees of partial melting caused by delamination of thickened lithospheric root (Pang et al., 2012, 2013b; Priestley et al., 2012).

The discrepancies above are primarily due to our limited knowledge of the structure, thermal condition, and composition of the lithospheric mantle beneath the Iranian Plateau. Xenoliths entrained within mantle-derived magmas are known to be fragments of the lower crust and lithospheric mantle, and therefore provide more "direct" constraints of the deep lithosphere. A recent study by Saadat and Stern (2012) documented a unique xenolith locality close to the triple junction between the Kopeh Dagh ranges, the Alborz Ranges, and the Sabzevar Zone, NE Iran (Fig. 1a). The abundance and variety of xenoliths in this locality provide a good opportunity to investigate the characteristics of the lithospheric mantle. In this paper, we present a detailed analysis of the petrology, mineralogy, and mineral chemistry of the mantle xenoliths to reveal the nature and deep processes of the lithospheric mantle beneath NE Iran and their implications for volcanic genesis and tectonic evolution.

2. Regional geology

The Iranian Plateau represents a part of the Alpine–Himalayan orogenic system and consists of an assemblage of lithospheric blocks separated by Paleozoic–Mesozoic ophiolite belts (Jannessary et al., 2012; Şengör et al., 1988; Zanchetta et al., 2013; Zarrinkoub et al., 2012). The plateau underwent several different tectonic episodes, resulting in complex and disparate tectonic domains, including the Central Iranian micro-continent in the centre surrounded by several active belts (Manaman et al., 2011). The Central Iranian micro-continent, consisting of, from east to west, the Lut, Tabas, and Yazd blocks (Fig. 1a), was accreted to the southern margin of Eurasia in the Late Triassic following the closure of the Paleotethys oceanic realm (Kaviani et al., 2009; Şengör and Natal'in, 1996; Shafiei et al., 2009; Zanchetta et al., 2013).

The Sistan Suture zone, eastern Iran marks the collision between the Lut and Afghan continental blocks presumably during the Late Cretaceous (Zarrinkoub et al., 2010). Remnants of the Paleotethys ocean are present in NE Iran, extending west into the Alborz Range and east to the Hindu-Kush in northern Afghanistan (Saadat and Stern, 2012). The Iranian Plateau then underwent continental collision with Arabia accompanied by the closure of the Neotethys ocean along what is now the Zagros suture (Fig. 1a). The timing of the collision event is controversial ranging from the Late Cretaceous to the Pliocene (Chiu et al., 2013; Dargahi et al., 2010; McQuarrie and van Hinsbergen, 2013; Pang et al., 2013b). The present-day convergence of Arabia and Eurasia in the Iranian Plateau is accommodated at collisional zones in Zagros, Alborz, and Kopeh Dagh and in subduction zones in the Makran basin (Fig. 1a; Kaviani et al., 2009; Manaman et al., 2011).

The continued subduction and collision events have altered the geophysical and geochemical properties of the lithosphere beneath the Iranian Plateau. The present-day convergence in Iran results in lithospheric thickening by axial shortening and vertical deformation (Allen et al., 2013; Kaviani et al., 2009; Manaman et al., 2011). Seismic imaging reveals that the SW Iran has the thickest lithosphere of ~260 km, and the lithosphere thickness abruptly decreases to <125 km

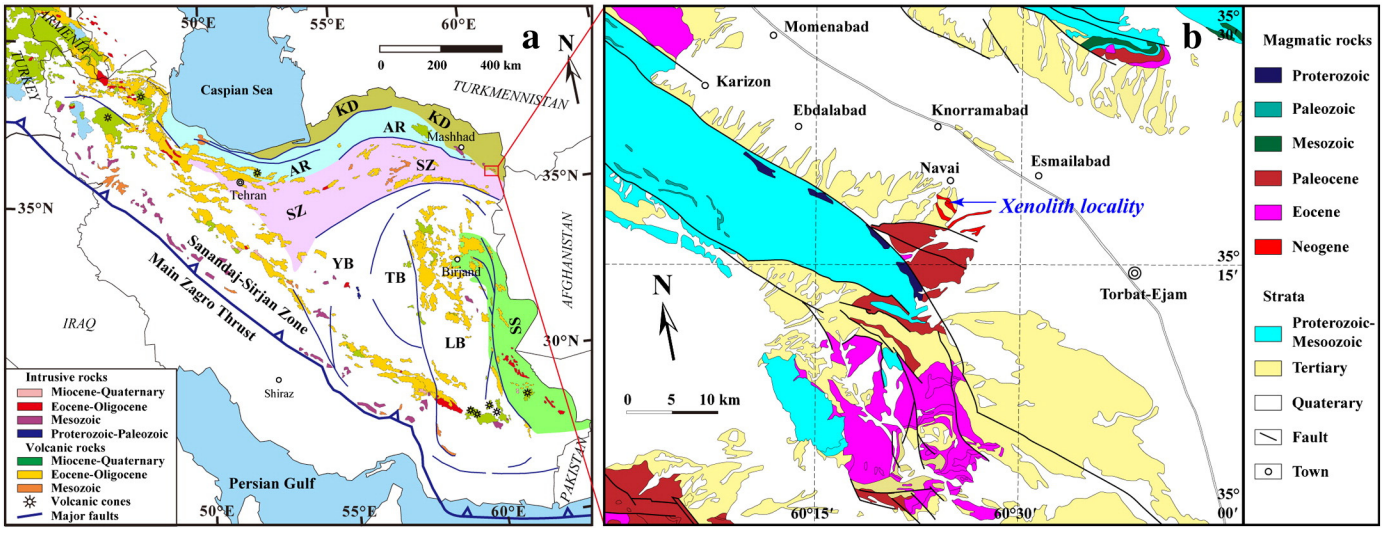

Fig. 1. (a) Simplified geological map showing the distribution of magmatic rocks in Iran and the major structural units of Iran (modified after Chiu et al., 2013; Jannessary et al., 2012). AR, Alborz Range; KD, Kopeh Dagh; LB, Lut Block; SS, Sistan Suture; SZ, Sabzevar Zone; TB, Tabas Block; YB, Yazd Block. (b) Geological map of the study area showing location of the xenoliths (after 1/250,000 geological map of Iran, Geological Survey of Iran).

in NE Iran (McKenzie and Priestley, 2008; Walker et al., 2009). Such a heterogeneous lithosphere is compatible with the distribution of Pliocene–Quaternary volcanism in the Iranian Plateau. As Walker et al. (2009) pointed out, Pliocene–Quaternary volcanic rocks are widespread in eastern and central Iran, but do not occur southwest of a NW–SE trending line to the north of the Main Zagros Thrust (Fig. 1a).

The Iranian Plateau is dominated by Eocene–Oligocene Andean-type volcanic rocks whose outcrops are broadly parallel to the sutures (Fig. 1a; Asiabanha and Foden, 2012; Chiu et al., 2013; Pang et al., 2013b; Verdel et al., 2011). These rocks are calc-alkaline to high-K calc-alkaline and are inferred to have originated from lithospheric mantle sources metasomatized by subduction-related fluid/melt (Alaminia et al., 2013; Asiabanha and Foden, 2012; Pang et al., 2013b). Volcanic activity during the Neogene appears to be less extensive than that of the Paleogene and is dominated by volumetrically minor alkali basaltic and ultrapotassic volcanism (Fig. 1a; Allen et al., 2013; Chiu et al., 2013; Kheirkhah et al., 2013; Liotard et al., 2008; Pang et al., 2012, 2013a; Saadat and Stern, 2012; Walker et al., 2009).

The study area is located near the Navai village about 150 km southeast from Mashhad, NE Iran (35°18'37.5'' N; 60°24'04.4'' E) (Fig. 1b), the same locality where Saadat and Stern (2012) documented a variety of crustal and mantle xenoliths. From a regional geology perspective, it occurs in the easternmost part of the Sabzevar Zone and the foot of the Kopeh Dagh ranges to the north where a Paleotethyan suture is presumably present. The xenoliths were found in a dome of alkali olivine basalt which, according to geological maps, erupted in the Neogene. They include peridotites, pyroxenites and granulites, and only the first two types of xenoliths are analyzed in this study. Surrounding the basalt dome are extensive Tertiary–Quaternary strata, consisting mainly of conglomerates and sandstones.

3. Petrography

Thirty two mantle xenoliths, including two dunites, 13 spinel lherzolites, 5 olivine websterites, 11 websterites and one clinopyroxenite, were investigated in this study. They mostly range in size from 1 to 4 cm across with a few up to ~7 cm and contain olivine, orthopyroxene, clinopyroxene and accessory spinel. The rocks are generally fresh without any obvious indication of reaction with the host basalts.

3.1. Dunite

The two dunites exhibit different mineral modes and textures. Sample 12-IR-ZS-84-32 (coarse-grained dunite) contains coarse-grained olivine (up to 0.8 cm in diameter) and rare spinel and clinopyroxene (Fig. 2a). The olivine is present as tabular or granular grains showing 120° triple junctions (Fig. 2b). They are often strained, exhibiting multiple kink bands and a set of ductile fractures (Fig. 2b, c). Spinel is present either as anhedral isolated grains or as rounded inclusions in the olivine (Fig. 2a, c). Two clinopyroxene grains were found in sample 12-IR-ZS-84-32. They exhibit a well-developed spongy texture (Fig. 2c), which is in striking contrast with the surrounding olivine and spinel, creating a well-defined boundary between each of the grains (Fig. 2c). In contrast, the sample 12-IR-ZS-84-39 (equigranular dunite) exhibits equigranular texture and contains a considerable amount of spinel (Fig. 2d, e). Most olivine grains in this sample are rounded in shape and do not develop kink band features, although triple junctions are observed (Fig. 2f). The spinel ranges in size from 100 to 250 μm and in most cases randomly dispersed, although it occasionally occurs between olivine grains (Fig. 2d, e), or less commonly setting along olivine fractures (Fig. 2f). The clinopyroxene in the sample 12-IR-ZS-84-39 is found as very tiny needles and has no spongy texture (Fig. 2e).

3.2. Spinel lherzolite

The spinel lherzolites are characterized by porphyroclastic and inequigranular textures with deformation features (Fig. 3a, b, c, d). Orthopyroxene porphyroclasts as large as 1 cm in length are present, and are commonly surrounded by a mosaic of equidimensional smaller grains of olivine and clinopyroxene (Fig. 3c). Spinel lamellae are occasionally observed in orthopyroxene porphyroclasts (Fig. 3c). In addition to the porphyroclasts, orthopyroxene is also present either as small, undulatory and anhedral grains in a mosaic arrangement, or as small, polygonal and undeformed grains (Fig. 3a, c, e). In many cases, the orthopyroxenes are highly deformed. The orientation of these orthopyroxene grains and sub-grains follows the general foliation of the samples (Fig. 3b, d).

The olivine in the spinel lherzolites is highly variable in size, ranging from >5 mm as interstitial grains to <1 mm as mosaic aggregates. The grains either display a kink banding (Fig. 3c, f) or are elongated to generate straight boundaries with adjacent minerals (Fig. 3d). Sets of fractures perpendicular to the direction of elongation commonly occur in the elongated olivine grains. The clinopyroxene is mostly anhedral and exhibits curved boundaries against adjacent orthopyroxene and olivine (Fig. 3e, f). The spongy texture found in other clinopyroxene grains is occasionally present in these samples. The texture is poorly developed or absent in the strongly deformed rocks (Fig. 3d, e, g), while it is typically present in the more weakly deformed samples (e.g., 12-IR-ZS-13; Fig. 3f, h). Melt pockets consisting of fine-grained olivine, clinopyroxene, and/or orthpyroxene are another prominent feature in some rocks (e.g., 12-IR-ZS-13 and 12-IR-ZS-25; Fig. 3f, h). In addition, accessory sulphides and plagioclase are occasionally observed among the major mineral grains or within the melt pockets, particularly in the weakly deformed spinel lherzolites.

3.3. Olivine websterite

The olivine websterite samples have a mineral assemblage of clinopyroxene, orthopyroxene, and olivine with or without accessory spinel, and generally display inequigranular and porphyroclastic texture (Fig. 4a, b, c). The clinopyroxene in these samples has a much larger grain size and a higher abundance than in the spinel lherzolite. They occur as subhedral or anhedral tabular grains and exhibit sub-grain boundaries with orthopyroxene and olivine (Fig. 4b, d). No spongy texture is observed in the clinopyroxene. The orthopyroxene occurs occasionally as large porphyroclasts surrounded by fine-grained olivine and clinopyroxene (Fig. 4c), but in most cases it is present as moderate to fine grains along the boundaries with clinopyroxene (Fig. 4e, f). The olivine in the olivine websterite samples varies widely in size and occurrence. The smaller, irregularly-shaped olivine grains are usually scattered between pyroxene grains (Fig. 4b, c), while the medium sized olivine grains occur interstitially and display curved contact relationships with the surrounding pyroxenes (Fig. 4d, f). It is noteworthy that some olivine grains in samples 12-IR-ZS-84-24 and 12-IR-ZS-84-33 exhibit weak iddingsitized features along cracks (Fig. 4d). The difference in contrast for both olivine and clinopyroxene in back-scattered images (i.e., Fig. 4e, f) reflects compositional variations between different samples.

3.4. Websterite

All websterite samples of this study are composed of dominant clinopyroxene and subordinate orthopyroxene with no spinel or olivine (Fig. 5a). Additional K-feldspar is also observed in a few samples (Fig. 5b). These websterites all exhibit an equigranular texture, and the pyroxenes are granular with sizes of 1–2 mm (Fig. 5a, c). The modal contents of the two pyroxenes vary among the websterites; for instance, 12-IR-ZS-84-10 has higher clinpyroxene abundance than the other samples. Triple junctions between equigranular clinopyroxene

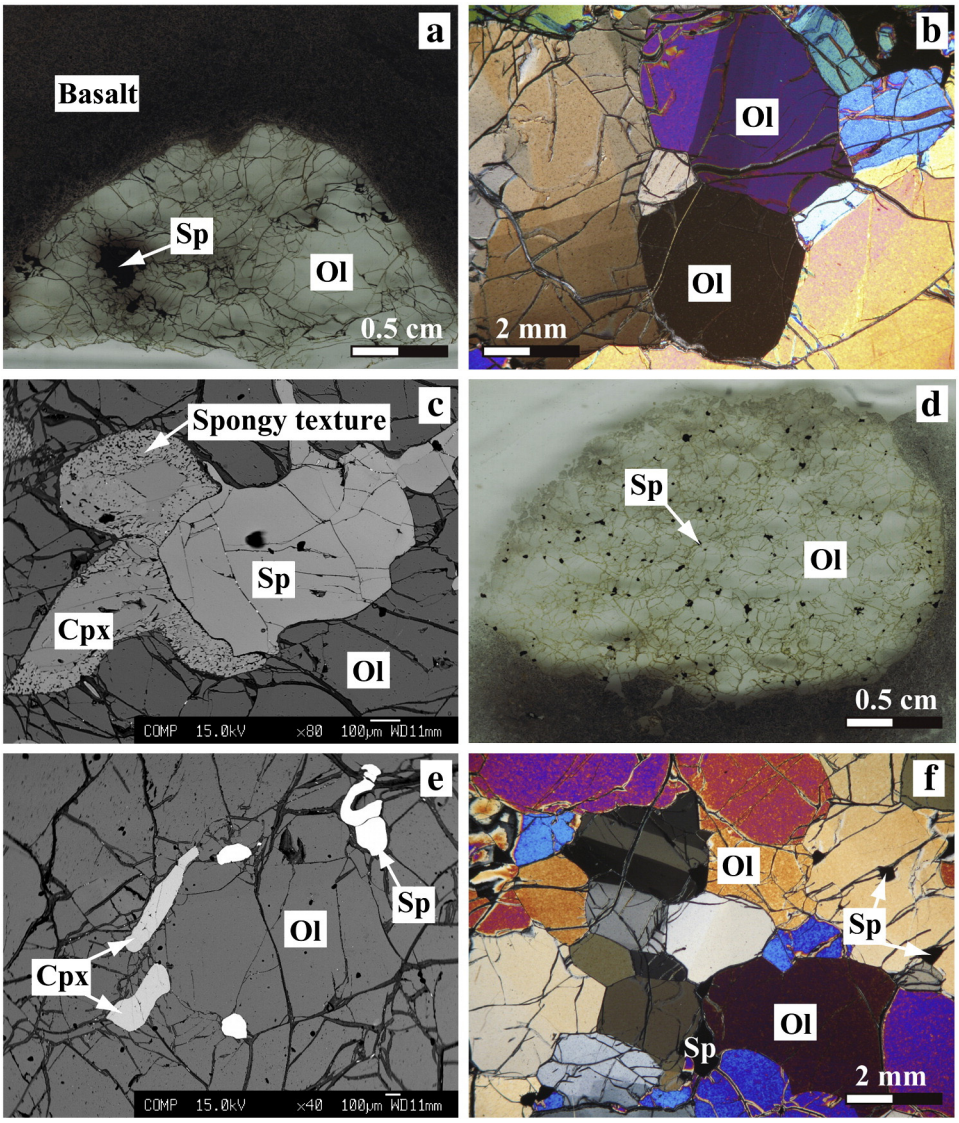

Fig. 2. Petrography of dunite xenoliths from NE Iran. (a) Coarse-grained olivine (Ol) and anhedral spinel (Sp) in sample 12-IR-ZS-84-32. (b) Granular olivine grains with kink band in sample 12-IR-ZS-84-32. (c) Spongy-textured clinopyroxene (Cpx) and anhedral spinel in sample 12-IR-ZS-84-32. (d) Equigranular texture of sample 12-IR-ZS-84-39. (e) Anhedral spinel and clinopyroxene occurring between olivine boundaries in sample 12-IR-ZS-84-39. (f) Granular olivine grains showing triple junction features in sample 12-IR-ZS-84-39.

and orthopyroxene are a common feature (Fig. 5c, d). Well-developed fractures are present in the pyroxene of sample 12-IR-ZS-84-36 (Fig. 5d).

3.5. Clinopyroxenite

The clinopyroxenite sample (12-IR-ZS-84-23) has a very similar texture to the websterites. It is made up almost entirely of clinopyroxene, with only one orthopyroxene grain found in the studied thin section.

4. Analytical methods

Major element analyses of the minerals were carried out at the Institute of Geology and Geophysics, Chinese Academy of Sciences, Beijing, China on carbon-coated polished thin sections using a JEOL JXA-8100 microprobe equipped with four wavelength-dispersive spectrometers and integrated with an energy-dispersive spectrometer system. Operating conditions include an accelerating voltage of 15 kV, a beam current of 10 nA, a beam size of 5 μm and a counting time of 10–30 s on each peak. For standard calibration, a variety of natural minerals were used: jadeite [$NaAlSiO_6$] for Na, Al, and Si, rhodonite [$MnSiO_3$] for Mn, sanidine [$KAlSi_3O_8$] for K, garnet [$Fe_3Al_2Si_3O_{12}$] for Fe, Cr-diopside [$(Mg, Cr)CaSi_2O_6$] for Ca, and olivine [$(Mg, Fe)_2SiO_4$] for Mg. A few synthetic minerals were also used: rutile [TiO_2] for Ti, 99.7% Cr_2O_3 for Cr, and Ni_2Si for Ni. The ZAF procedure was used for matrix corrections. The precision for all analyzed elements is better than 98.5%. The analytical results of each mineral represent at least 3 spot analyses of several grains from different parts of each sample.

In-situ trace element concentrations were measured using laser ablation inductively-coupled plasma mass spectrometry (LA-ICP-MS) at the China University of Geosciences, Wuhan. Detailed analytical procedures are described elsewhere (Liu et al., 2008). Helium was used as a carrier gas to enhance the transport efficiency of the ablated sample. The helium carrier gas inside the ablation cell was mixed with argon, acting as a makeup gas, before entering the ICP in order to maintain the stable and optimum excitation condition. The measurements were carried out using time resolved analysis operating in a fast, peak-hopping sequence in dual detector mode. A 40 μm spot size was used in this study. Each spot analysis consisted of approximately 30 s of background acquisition followed by 60 s of data acquisition. Calibration was performed using NIST SRM 610 as an external calibration sample together with Si as an internal standard element (Chen et al., 2011; Liu et al., 2008).

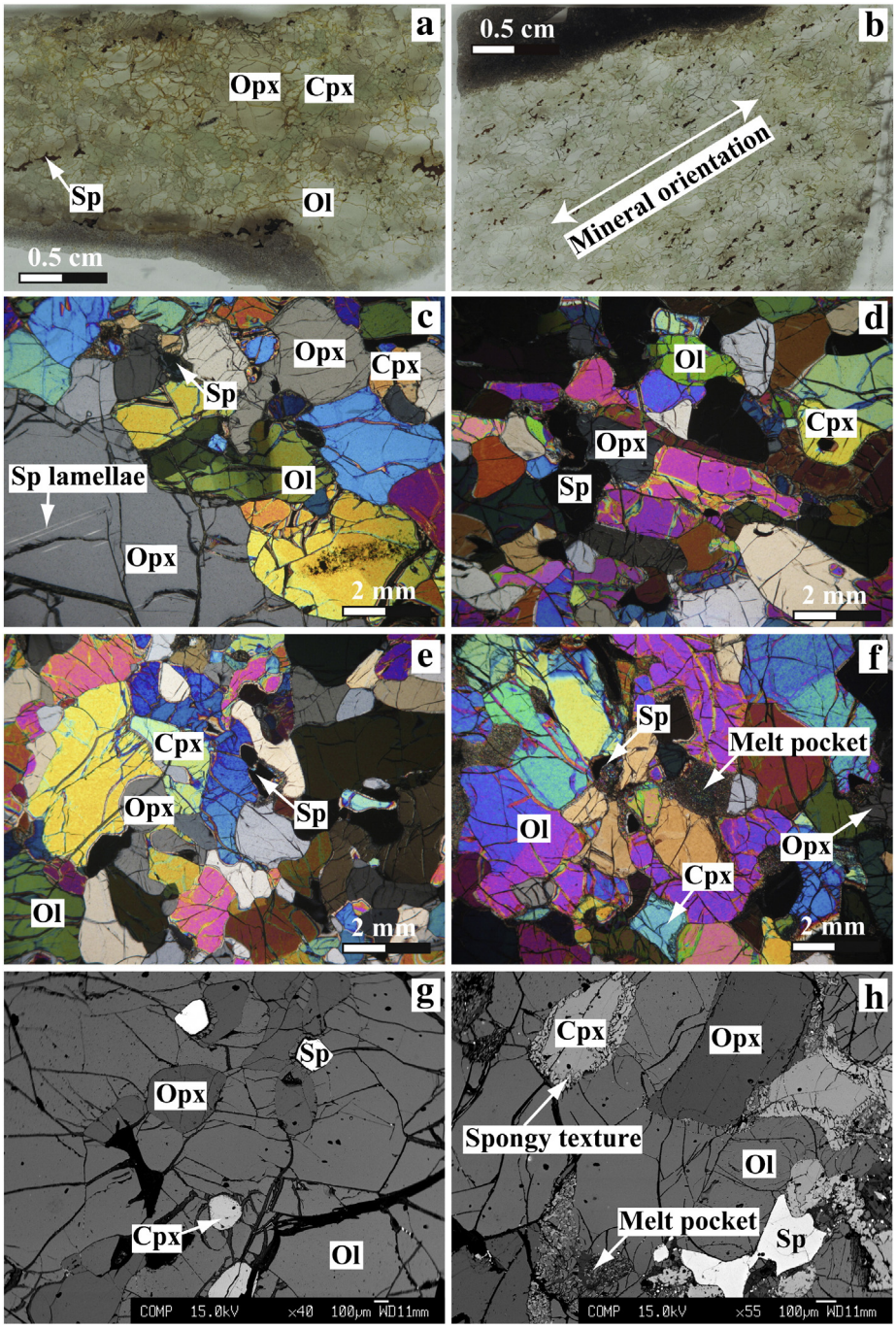

Fig. 3. Petrography of spinel lherzolite xenoliths from NE Iran. (a) Sample 12-IR-ZS-84-35 showing porphyroclastic texture and containing porphyroclastic orthopyroxene (Opx), inequigranular olivine, anhedral clinopyroxene and spinel. (b) Mineral elongation and orientation features in sample 12-IR-ZS-84-12. (c) Porphyroclastic orthopyroxene containing spinel lamellae and surrounded by olivine and clinopyroxene with varying grain sizes in sample 12-IR-ZS-84-35; some olivine, clinopyroxene and spinel grains are broken into pieces. (d) Mineral deformation and elongation features in sample 12-IR-ZS-84-09. (e) Curved boundaries between the major minerals in sample 12-IR-ZS-84-37. (f) Deformation and curved boundaries between the major minerals, and the occurrence of a melt pocket in sample 12-IR-ZS-84-27. (g) Fine-grained and granular orthopyroxene and spinel between olivine and clinopyroxene in sample 12-IR-ZS-84-37. (h) Spongy-textured clinopyroxene associated with a melt pocket in sample 12-IR-ZS-84-13.

5. Results

5.1. Major elements

5.1.1. Olivine

The olivines in the dunite and spinel lherzolite samples have similar compositions in Fo (forsterite), MnO and NiO contents (Appendix Table 1S), and cluster in the field of non-cratonic peridotite as defined by Walter (2003) (Fig. 6a, b). The equigranular olivines in sample 12-IR-ZS-84-39 show slightly lower NiO contents than the coarse-grained olivines in sample 12-IR-ZS-84-32. The fine olivine grains found in the mosaic aggregates of orthopyroxene porphyroclasts in the spinel lherzolites have different compositions, i.e., low NiO contents, high MnO and CaO (Fig. 6a, b; Appendix Table 1S), indicating that they were recrystallized. The olivines in samples 12-IR-ZS-84-13 and 12-IR-ZS-84-19 have lower Fo and higher MnO relative to those in the other spinel lherzolites, which mean that they are shifted away from the non-cratonic peridotite field.

The olivines in the olivine websterite samples display large compositional variations (Appendix Table 1S). Overall, MnO and NiO are in

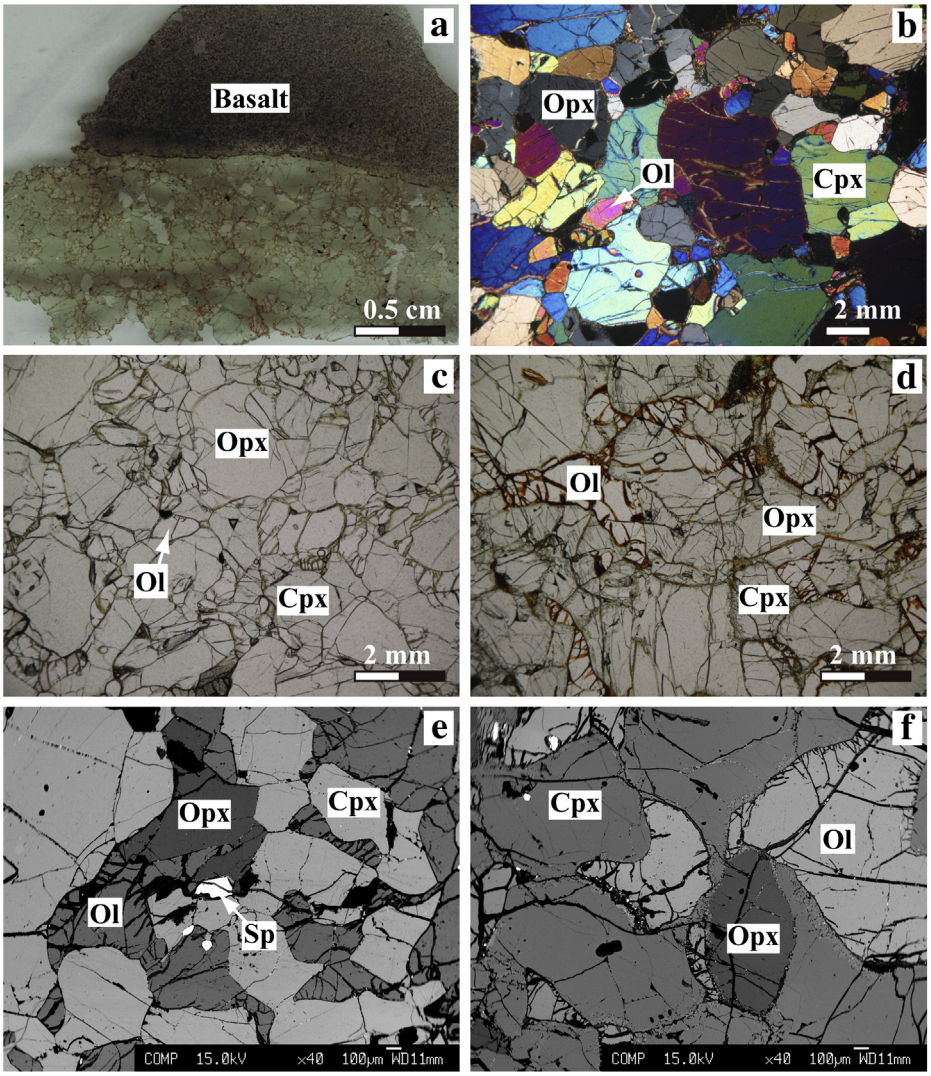

Fig. 4. Petrography of olivine websterite xenoliths from NE Iran. (a) Inequigranular texture in sample 12-IR-ZS-84-38. (b) Inequigranular clinopyroxene and orthopyroxene with fine-grained olivine in sample 12-IR-ZS-84-33. (c) Porphyroclastic texture in sample 12-IR-ZS-84-38 showing porphyroclastic orthopyroxene surrounded by fine-grained olivine and clinopyroxene. (d) Olivines in sample 12-IR-ZS-84-24 exhibiting weak iddingsitized feature along fractures. (e) Sample 12-IR-ZS-84-38 consisting of clinopyroxene and orthopyroxene with minor olivine and small amounts of spinel. (f) Curved contact relationship between the major minerals in sample 12-IR-ZS-84-24.

negative and positive correlation with Fo, respectively (Fig. 6a, b). They mostly plot within or close to the pyroxenite xenoliths field (Zhang et al., 2010a) and are compositionally different from the pyroxenite cumulates worldwide (Fig. 6a, b; Walter, 2003; Zheng et al., 1998).

5.1.2. Orthopyroxene

The compositions of the orthopyroxene are completely different between the spinel lherzolites and the pyroxenites (Fig. 6c, d). The orthopyroxene in the spinel lherzolites has low FeO (5.5–9.0 wt.%), high Al_2O_3 (3.3–5.5 wt.%) contents, and a high Mg# ($100 \times Mg/(Mg + Fe)$; 90–91.5) (Appendix Table 1S). Among the spinel lherzolites, two samples (12-IR-ZS-84-13 and 12-IR-ZS-84-19) display orthopyroxene compositions with relatively low Mg# (Fig. 6c, d). The orthopyroxenes in the pyroxenite samples exhibit large compositional variations (Appendix Table 1S). Overall, the major oxides are well correlated with Mg# numbers (Fig. 6c, d). There is no significant difference in CaO contents between the spinel lherzolites and the pyroxenites.

5.1.3. Clinopyroxene

Like the orthopyroxenes, the clinopyroxenes in the spinel lherzolites have different compositions than the clinopyroxenes in the pyroxenites (Fig. 7). The clinopyroxenes in the spinel lherzolites have restricted ranges of Al_2O_3 and Mg#, placing them in the non-cratonic peridotite field (Fig. 7a; Walter, 2003). Two samples (12-IR-ZS-84-13 and 12-IR-ZS-84-19) have clinopyroxenes with considerably lower Mg#s and similar variations in other major oxide compared to other spinel lherzolites. In contrast, the clinopyroxenes in the pyroxenites show larger compositional variations. For instance, their Mg# and Cr# ranges from 80 to 91 and 3 to 21, respectively (Fig. 7b). These clinopyroxenes display good correlations between the major oxides and Cr# and Mg# (Fig. 7a, b, c). The clinopyroxenes from the olivine websterites exhibit generally higher Mg# and Cr# and lower Al_2O_3 and TiO_2 contents than those from the websterites. The clinopyroxenes from the clinopyroxenite have a moderate Mg# and Cr# and the highest Na_2O contents (Fig. 7d). The coarse-grained dunite sample (12-IR-ZS-84-32) contains clinopyroxenes similar in composition to those from the spinel lherzolites. The clinopyroxenes in the dunite sample 12-IR-ZS-84-39 are totally distinct from the dunite sample 12-IR-ZS-84-32 and the spinel lherzolites, containing low Al_2O_3 and TiO_2, and a high Cr#. However, these clinopyroxenes can be linked to pyroxenites when the effects of metasomatism are taken into account (Fig. 7).

The fine-grained clinopyroxenes from mosaic aggregates of orthopyroxene porphyroclast in the spinel lherzolites contain more SiO_2 and have a higher Cr#, although they have lower levels of TiO_2,

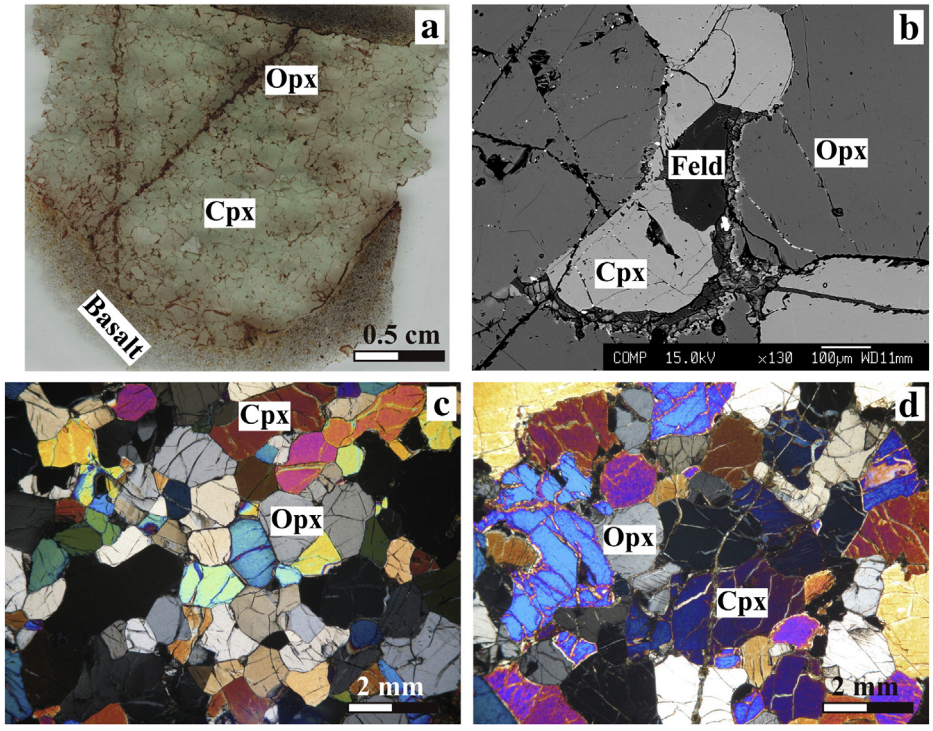

Fig. 5. Petrography of websterite xenoliths from NE Iran. (a) Equigranular texture in sample 12-IR-ZS-84-34. (b) K-feldspar (Feld) between clinopyroxene and orthopyroxene in sample 12-IR-ZS-84-10. (c) Triple junction between equigranular clinopyroxene and orthopyroxene in sample 12-IR-ZS-84-10. (d) Well-developed fractures in clinopyroxene and orthopyroxene in sample 12-IR-ZS-84-36.

Al_2O_3 and Na_2O (Appendix Table 1S). As for the spongy-textured clinopyroxenes, from spongy rim to core, the general trend is an increase in Al_2O_3 and Na_2O and a decrease in TiO_2 and Cr# (Appendix Table 1S).

5.1.4. Spinel

The spinels in the spinel lherzolites display a homogeneous composition, although both 12-IR-ZS-84-13 and12-IR-ZS-84-19 contain spinels with a slightly lower Mg# (65–75). They have narrow ranges of

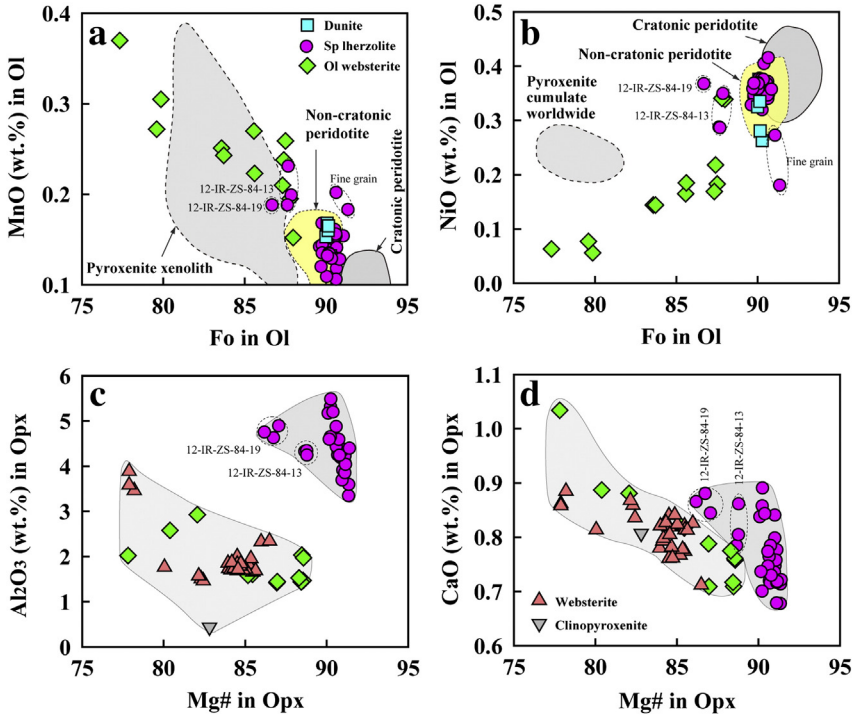

Fig. 6. Fo vs. MnO (a) and Fo vs. NiO (b) plots for olivine and Mg# vs. Al_2O_3 (c) and Mg# vs. CaO (d) plots for orthopyroxene in mantle xenoliths from NE Iran. The fields for cratonic and non-cratonic peridotites are from Walter (2003). The pyroxenite xenolith field is from Zhang et al. (2010a). The pyroxenite cumulate worldwide field is defined based on the data from Zheng et al. (1998) and Walter (2003).

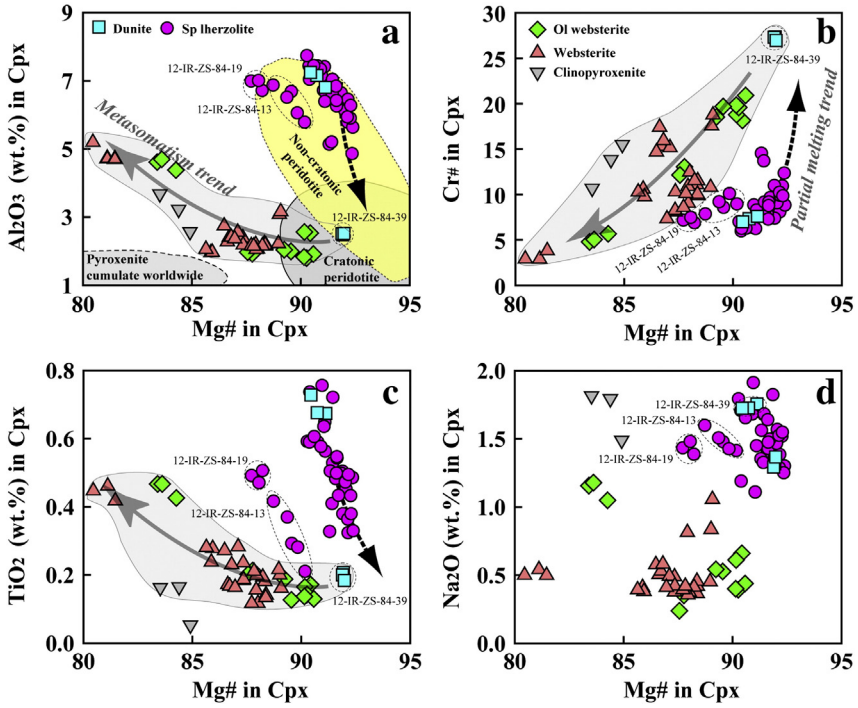

Fig. 7. Mg# vs. Al_2O_3 (a), Cr# (b), TiO_2 (c), and Na_2O (d) plots for clinopyroxene in mantle xenoliths from NE Iran. Spongy composition is not shown in the plots. The fields for cratonic and non-cratonic peridotites and the pyroxenite cumulate worldwide are from Walter (2003).

Cr# (8–17; except for the samples 12-IR-ZS-84-37) and TiO_2 (0.05–0.22 wt.%) and high Mg# (76–80) (Appendix Table 1S; Fig. 8). The composition of the spinel grains in the coarse-grained dunite (12-IR-ZS-84-32) overlaps that of the spinel lherzolites, and they are all comparable to the spinels from non-cratonic peridotites worldwide (Fig. 8a; Rudnick et al., 2004). Spinels from the equigranular dunite sample (12-IR-ZS-84-39) and the olivine websterites have a relatively high Cr# and high TiO_2 contents, but a lower Mg# than those in the other groups (Appendix Table 1S; Fig. 8).

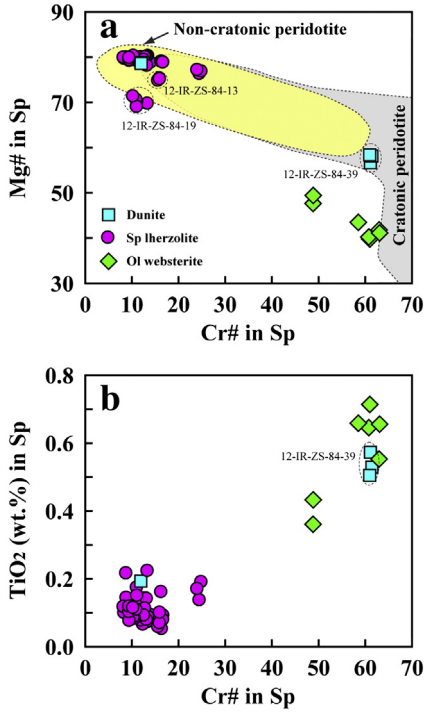

Fig. 8. Cr# vs. Mg# (a) and Cr# vs. TiO_2 (b) plots for spinel in mantle xenoliths from NE Iran. The fields for non-cratonic and cratonic peridotites are from Rudnick et al. (2004).

5.2. Trace elements in clinopyroxene

We conducted two spot analyses on two clinopyroxene grains from each sample. The results reveal that the clinopyroxenes in each individual sample have a rather uniform trace element composition (Appendix Table 2S; Fig. 9). Distinct trace element patterns, however, are present among different rock types or even within the same group. The two clinopyroxenes from the coarse-grained dunite (12-IR-ZS-84-32) exhibit depletion in light rare earth elements (LREE) and a flat heavy REE (HREE) distribution in chondrite-normalized REE patterns (Fig. 9a). They have similar abundances of most incompatible trace elements to the primitive mantle, with the exception of large ion lithophile elements (LILE) (Fig. 9b; Sun and McDonough, 1989). In contrast, the clinopyroxenes in the equigranular-textured dunite sample (12-IR-ZS-84-39) show overall high trace element concentrations, high LREE-HREE fractionation with LREE enrichment, and negative Ba, Nb, Ta, Pb, and Ti, with slight Zr and Hf anomalies (Appendix Table 2S; Fig. 9a, b).

The clinopyroxenes in all but one of the spinel lherzolite samples display consistent trace element patterns with variable LREE and LILE concentrations (Fig. 9c, d; Appendix Table 2S). They all have LREE depletion with flat HREE patterns and slight negative Zr and Hf anomalies. The negative anomalies in Ba, Nb, Ta, Pb, and Ti are more prominent than those in the dunites. The concentrations of most incompatible trace elements are similar to those of the primitive mantle (Fig. 9d; Sun and McDonough, 1989). The LREE-enriched clinopyroxenes are from the sample 12-IR-ZS-84-13 (Fig. 9c). The plagioclase-bearing sample (12-IR-ZS-84-25) contains the clinopyroxenes with the highest Th and U abundances (Appendix Table 2S; Fig. 9d).

The clinopyroxenes in the olivine websterite samples show variable trace element compositions. The clinopyroxenes in the sample 12-IR-ZS-84-24 have the highest trace element concentrations and display similar REE and trace element patterns to those of the spinel lherzolite

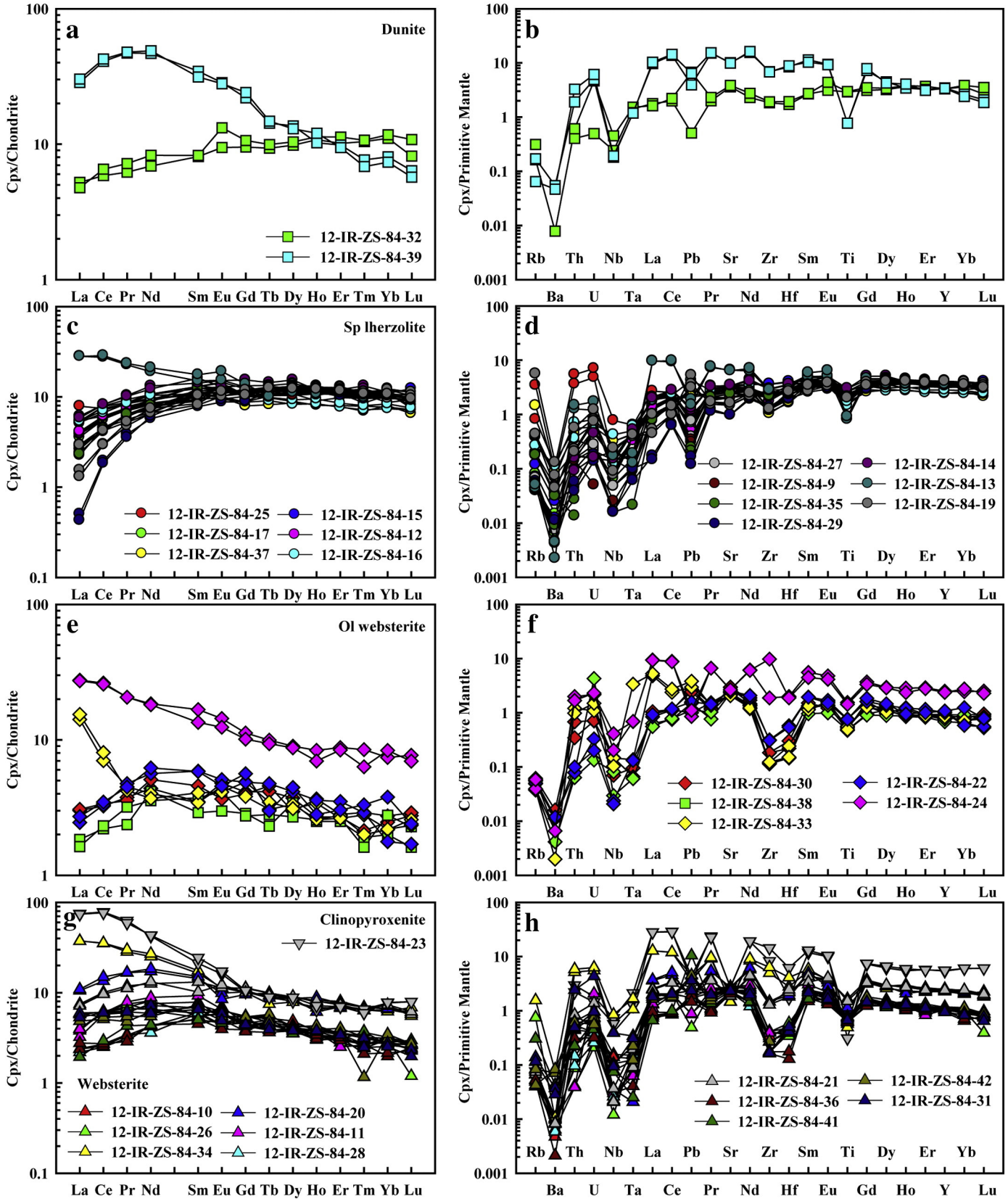

Fig. 9. Chondrite-normalized rare earth element and primitive mantle-normalized trace element patterns for clinopyroxene in mantle xenoliths from NE Iran. The chondrite and primitive mantle values are from Anders and Grevesse (1989) and Sun and McDonough (1989), respectively.

sample 12-IR-ZS-84-13 (Appendix Table 2S; Fig. 9e, f). The clinopyroxenes from another four olivine websterites are characterized by similar moderate or heavy REE concentrations and patterns, depletions in Rb, Ba, Pb, Ti and in the high field strength elements (HFSE: Nb, Ta, Zr, Hf), as well as positive Sr anomalies, although sample 12-IR-ZS-84-33 displays LREE enrichment.

Unlike other rock types, the clinopyroxenes in all of the websterites appear to be slightly enriched in LREE and have fractionated REE patterns (Fig. 9g, h). The Ba, Ti, and HFSE depletions are more considerable and consistent in the websterites. The Sr and Pb anomalies are variable, being positive in some samples and negative in others. The clinopyroxenite has clinopyroxenes with significant LILE depletion and the highest trace element concentrations among all the samples in this study (Appendix Table 2S; Fig. 9g, h).

6. Discussion

The petrological and mineral chemical variations of the dunites, spinel lherzolites, and pyroxenites indicate that a variety of processes occurred at depth were involved in their formation. This dataset provides constraints on these deep processes and on the nature of the lithospheric mantle beneath NE Iran. In the following sections, we will discuss the primitive mantle-like composition, subduction-related metasomatism, low-degree partial melting, mantle deformation and thermal condition, and the structure of the lithosphere in this region, as well as the tectonic implications for this convergent zone.

6.1. Primitive mantle-like composition

The spinel lherzolites from the lithospheric mantle beneath NE Iran are mostly composed of olivine, orthopyroxene with high Al_2O_3, and clinopyroxenene with high Al_2O_3 and low TiO_2 (Appendix Table 1S; Figs. 6–8). These rocks are of typical non-cratonic peridotite and are comparable to primitive mantle compositions (Figs. 6, 7, 8). Mapping of Fo content in olivine from the lithospheric mantle reveals a decrease in the mean Fo of olivine with its age: from Archean (Fo = 92–94) through Proterozoic (Fo = 90.5–92.5) to Phanerozoic (Fo = 88.5–91.5) (Gaul et al., 2000; Griffin et al., 1999). The lithospheric mantle beneath NE Iran has low Fo olivine (Fo = 90–91), probably indicating that it formed during the Phanerozoic. This inference is further supported by its non-cratonic peridotite composition which is representative of newly-accreted lithospheric mantle (Walter, 2003). In terms of trace elements, the clinopyroxenes in the spinel lherzolites and in one dunite sample (12-IR-ZS-84-32) display flat REE with mild LREE depletion and incompatible trace element patterns parallel to the primitive mantle (Fig. 10a, b). The most incompatible trace element concentrations of these clinopyroxenes are also close to the primitive mantle abundances (Appendix Table 2S; Fig. 10a, b). These features may indicate that the lithospheric mantle beneath NE Iran is compositionally similar to the primitive mantle, except for limited inconsistent depletions of LREE and LILE (Figs. 9, 10). This may be attributed to a low degree of partial melting and mantle metasomatism (Griffin et al., 1999; Walter, 2003; Zheng et al., 1998).

6.2. Subduction-related mantle metasomatism and the genesis of the pyroxenites

Although most of the spinel lherzolites and the coarse-grained dunite resemble the primitive mantle in composition, two spinel lherzolites (12-IR-ZS-84-13 and 12-IR-ZS-84-19) and the equigranular dunite display distinctly different compositional features. The characteristically lower Mg# of olivine, orthopyroxene, clinopyroxene, and spinel in both of these spinel lherzolites, as well as the LREE enrichments of clinopyroxene in samples 12-IR-ZS-84-13 and 12-IR-ZS-84-39 (Figs. 6–9), indicates that they have undergone considerable refertilization (Zheng et al., 1998). Further, the variably negative HFSE

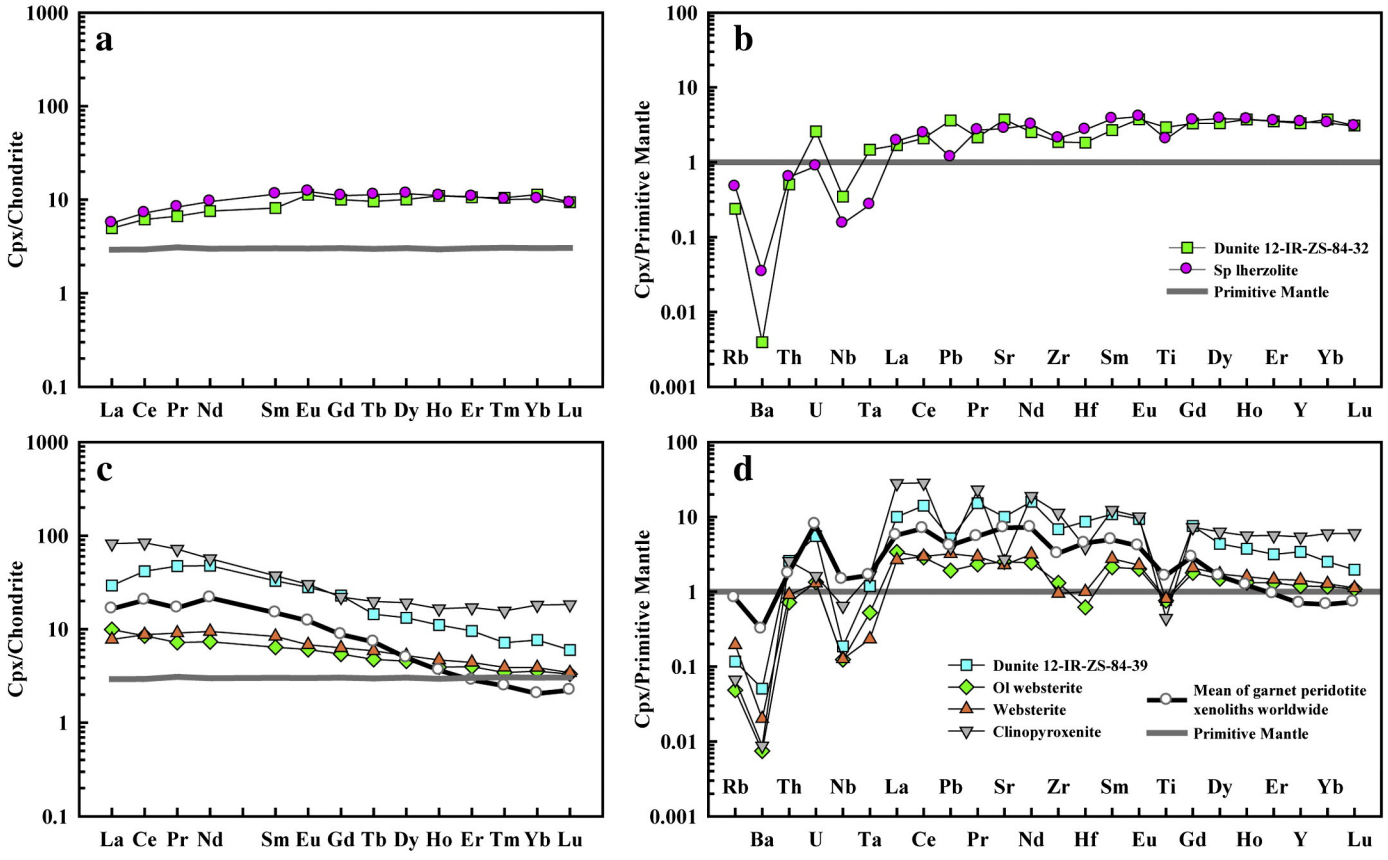

Fig. 10. The average trace element compositions of clinopyroxene in mantle xenoliths from NE Iran compared to the primitive mantle (Sun and McDonough, 1989) and clinopyroxenes in garnet peridotite xenoliths worldwide (Su et al., 2011a; and references therein). (a) and (c) are normalized to chondrite (Anders and Grevesse, 1989) and (b) and (d) are normalized to PM (Sun and McDonough, 1989).

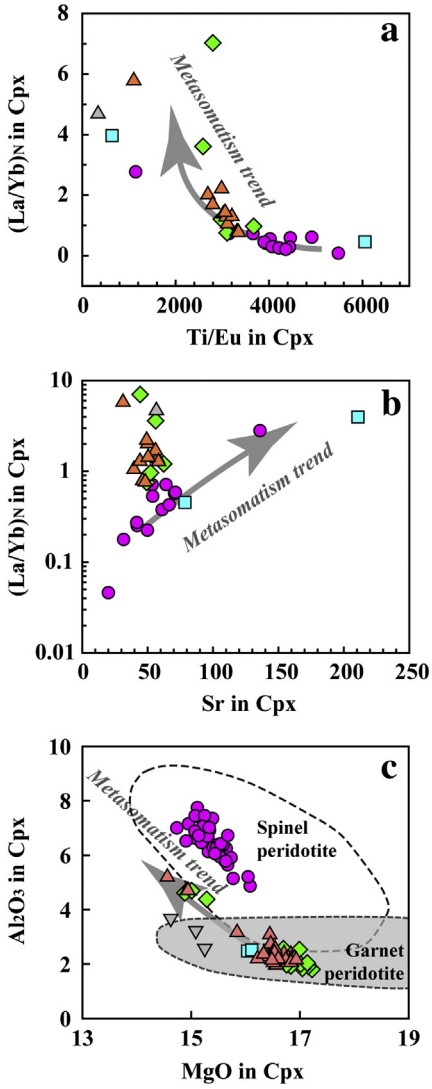

Fig. 11. Ti/Eu (a) and Sr (b) vs. $(La/Yb)_N$ (primitive mantle-normalized; Sun and McDonough, 1989) and MgO vs. Al_2O_3 (c) plots for clinopyroxene in mantle xenoliths from NE Iran. The data used in plots a, b and c are the average values for clinopyroxene in Appendix Tables 1S and 2S, and all of the analytical data are used for plot (c). Legends are the same as in Fig. 7. The spinel and garnet peridotite fields are after Rudnick et al. (1993).

anomalies in clinopyroxene of all of the spinel lherzolites point to melt modification (Fig. 9d). Mantle metasomatism would considerably increase the La/Yb ratio and the incompatible trace element concentrations, while decreasing the Ti/Eu ratio (e.g., Gorring and Kay, 2000; Rudnick et al., 1993; Zheng et al., 1998). High $(La/Yb)_N$ (primitive mantle normalized) and low Ti/Eu ratios in clinopyroxene from the NE Iranian spinel lherzolites and pyroxenites clearly indicate metasomatism (Fig. 11a). Lithium has also been recognized as a sensitive metasomatic indicator (e.g., Woodland et al., 2004), and Li contents >5 ppm (Appendix Table 2S) can cause metasomatic effects (e.g., Su et al., 2012, 2014; Woodland et al., 2004; Zhang et al., 2010b). In addition, melt pockets in some of the spinel lherzolites (e.g., samples 12-IR-ZS-84-27 and 12-IR-ZS-84-13; Fig. 3f, h) are clear evidence for the existence of metasomatic melts (Ionov et al., 1993; Su et al., 2010; Szabo et al., 1996).

Numerous studies have been conducted on diverse pyroxenites, as they are ubiquitously distributed in the upper mantle and do not only influence mantle heterogeneity but also act as inferred source materials of ocean island basalts and mid-ocean ridge basalts (Frets et al., 2012; Herzberg, 2011; Sobolev et al., 2005; Ying et al., 2013; Zhang et al., 2010b). The genesis of mantle pyroxenites is traditionally divided into three categories: high pressure cumulates from basaltic magmas passing through the mantle, solid-state remnants of subducted oceanic crust and metasomatic products resulting from the interaction of pervasive melts with mantle peridotites (Herzberg, 2011; Sobolev et al., 2005; Ying et al., 2013; Zhang et al., 2010b). The compositions of olivine and clinopyroxene from the pyroxenites in this study (Figs. 6, 7a) rule out the possibility of a cumulate origin. The possibility of remnant oceanic crust is also unlikely because the pyroxenites from NE Iran have such diverse compositions and petrological features (i.e., recrystallization and triple junctions, as well as relict fine-grained olivine). Hence mantle metasomatism is the preferred explanation for the genesis of the Iranian pyroxenites since they show metasomatic signatures in trace element diagrams.

Mantle metasomatism creates enrichments in incompatible major elements (e.g., Al_2O_3, CaO, and TiO_2) in minerals (e.g., Rudnick et al., 1993, 2004; Walter, 2003; Zheng et al., 1998). These major element compositions (oxides) in mineral constituents of the pyroxenites are well correlated, illustrating a clear metasomatic trend (Figs. 6–8). In clinopyroxene from the pyroxenites, the $(La/Yb)_N$ ratio is larger and the Ti/Eu ratio is lower than those in the clinopyroxene of the spinel lherzolites, which clearly indicats that the pyroxenites have experienced a higher degree of metasomatism. The clinopyroxenite has the highest clinopyroxene trace element concentrations. The websterites usually have moderate trace element concentrations, somewhere between the olivine websterite and clinopyroxenite values. These compositional variations, together with decreasing olivine contents, and orthopyroxene and spinel modal contents, suggest that the degree of metasomatism increases from olivine websterite through websterite to clinopyroxenite. Taking all the metasomatized rocks into account, the equigranular dunite (12-IR-ZS-84-39) can be considered a metasomatic member in the genesis of the pyroxenites. The dunite may have experienced prior partial melting, as evidenced by the slightly higher Mg# in olivine and clinopyroxene, lower Al_2O_3 and TiO_2 contents in clinopyroxene, and extremely high Cr# in clinopyroxene and spinel (Figs. 6, 7, 8). The subsequent metasomatism then has resulted in the dunite falling along the metasomatism trend of the pyroxenites, having similar trace element patterns.

However, these metasomatism trends, especially those for orthopyroxene and clinopyroxene, are different from the spinel lherzolite trend (Figs. 6, 7). In the Sr vs. $(La/Yb)_N$ plot for clinopyroxene, the pyroxenites have a lower Sr value for a given $(La/Yb)_N$ ratio than that is evident in the metasomatism trend defined by the spinel lherzolites (Fig. 11b). Furthermore, there are only a few similarities in trace element patterns between the pyroxenites and spinel lherzolites (Fig. 9). This indicates that the pyroxenites might not be derived from the spinel lherzolites. Generally, spinel and olivine are completely absent in the websterites and clinopyroxenite, implying that the protolith of most but not all pyroxenites is not spinel-facies peridotite. On the other hand, the pyroxenites and the equigranular-textured dunite are similar to the worldwide garnet peridotites in regard to their trace element concentrations and patterns of clinopyroxenes (Fig. 10c, d; Su et al., 2011a) having fractionated REE with LREE enrichment, LILE depletion, and negative Ba, Nb, Ta, Pb, Zr, and Ti anomalies (Fig. 10a, d). The HREE enrichments in the pyroxenites and the equigranular dunite vary relative to the worldwide garnet peridotites, but those differences may be related to the extent of the metasomatism. The Al_2O_3 content is sensitive to pressure and temperature, and therefore can often effectively distinguish spinel- and garnet-facies peridotites (Nimis and Taylor, 2000; Rudnick et al., 1993). In the MgO vs. Al_2O_3 plot for clinopyroxene, the equigranular-textured dunite and most pyroxenites fall in the garnet peridotite field, and the defined metasomatic trend shifts away from the spinel peridotite field (Fig. 11c). These features are in agreement with the higher pressure estimates for the pyroxenites than those for the spinel lherzolites (shown below), suggesting that the

pyroxenites may have originated at a greater depth. It is thus reasonable to infer that the genesis of the pyroxenites, and most likely some of the dunites, is a metasomatized garnet-facies peridotite protolith.

The pronounced LREE enrichment and significant Nb, Ta, Pb, Zr, Hf, and Ti anomalies in the clinopyroxenes from most of the studied pyroxenites (Fig. 9f, h) imply that the metasomatic melts are probably linked to subducted oceanic lithosphere (Allen et al., 2013; Pang et al., 2012; Ying et al., 2013; Zhang et al., 2010a; Zindler and Hart, 1986). Many studies have documented that Cenozoic mantle-derived magmatism in the Iranian Plateau often preserves relics of the subducted slab, since the rocks mostly originate from slab-derived metasomatized sources (Alaminia et al., 2013; Allen et al., 2013; Asiabanha and Foden, 2012; Mirnejad et al., 2010; Pang et al., 2013b; Priestley et al., 2012). The subducted materials are either from the Paleotethys or Neotethys ocean, but due to a lack of isotopic data, one cannot yet determine which. In NE Iranian xenoliths, the general absence of hydrous minerals such as phlogopite and amphibole (though Saadat and Stern (2012) found amphibole in one sample) and presence of plagioclase/feldspar as a metasomatized mineral phase (Fig. 5b; Appendix Table 1S) suggest that the reactive melts were anhydrous or water-poor (Niu, 2005). Consequently, these melts may have been generated by the melting of a stagnated slab that had experienced dehydration during subduction (Manaman et al., 2011; Motaghi et al., 2012a). Therefore, the lithospheric mantle beneath NE Iran has undergone upward metasomatism, larger degree in garnet-facies rather than spinel-facies peridotite, caused by upwelling melts from the melting of the stagnated slab.

6.3. Mantle deformation and low partial melting

Lithospheric deformation commonly occurs in orogenic belts and is accommodated mostly by axial shortening, lateral shearing, striking slip faulting, etc. The visually and geophysically detectable deformation is relatively limited within the crustal level compared to within the lithospheric mantle. Numerous investigations of the Iranian Plateau have demonstrated that the strong crustal deformation caused by the Arabian–Eurasian continental collision has led to high levels of seismicity and many geophysical anomalies (Amini et al., 2012; Kaviani et al., 2009; Maggi and Priestley, 2005; Mottaghi et al., 2013). Whether the lithospheric mantle underneath the plateau has been deformed is still unclear. The deformation in the lithospheric mantle in the Iranian orogenic belts (Alborz, Zagros, and Kopeh-Dagh) has been assumed based on the null measurements of shear wave splitting, which are interpreted to be dominated by vertical rather than horizontal deformation associated with axial shortening (Kaviani et al., 2009). This study provides clear evidence for mantle deformation in NE Iran, based on the observed porphyroclastic texture and mineral elongation in the Iranian xenoliths, which are typical deformation features in mantle peridotites (Fig. 3). The kink-banded olivine, curved mineral boundaries and mineral orientations demonstrate strong shear strain in the lithospheric mantle, which may account for the seismic anisotropy (e.g., Gaul et al., 2000; Hansen et al., 2014; Kaviani et al., 2009). Because the deformation features are only present in the spinel lherzolites, the deformation in the study area is probably limited to <70 km and does not extend throughout the whole lithosphere. The presence of orthopyroxene porphyroclasts surrounded by fine-grained high-Mg minerals (Figs. 3a, c, 6; Appendix Table 1S) suggests that deformation was accompanied by local recrystallization and small degree of partial melting (Allen et al., 2013). An alternative explanation for the absence of deformation in the pyroxenite xenoliths could be that they were crystallized after the deformation event.

In the study area, three episodes of partial melting in the lithospheric mantle can be identified. The earliest stage is represented by the equigranular dunite. The partial melting in this stage may be of high degree, as indicated by very low NiO in olivine, low Al_2O_3 and TiO_2, and high Mg# and Cr# in clinopyroxene, and high Cr# in spinel (Figs. 6b, 7a, b, c, 8).

The second episode of partial melting has most likely occurred after mantle metasomatism. Both processes are likely of large scale, occurring throughout the lithospheric mantle. The major elemental variations within the pyroxenes, particularly the clinopyroxenes, in the spinel lherzolites indicate partial melting trends (Figs. 6, 7). The most incompatible LREE and LILE become depleted in clinopyroxenes (Fig. 9c, d). The clinopyroxenes in the olivine websterites are depleted in LILE with positive or negative LREE depletion, although only LILE depletion appears in websterites and clinopyroxenites that preserve variable LREE enrichment (Figs. 9, 10). These features vary between different rock types suggesting that the degree of partial melting is relatively low and decreases downward from spine-facies to garnet-facies mantle. According to this scenario, the melting might not be induced by elevated temperature, but by the shallow extensional setting, which is in agreement with previous studies (e.g., Pang et al., 2013b; Verdel et al., 2011; Zarrinkoub et al., 2010). Several authors have proposed an early to mid-Tertiary extensional tectonic regime resulting in the development of metamorphic core complexes in central and northern Iran (Verdel et al., 2011 and references therein). The regime in eastern Iran also played a crucial role in the generation of Eocene–Oligocene calc-alkaline volcanism in the Lut Block and Sistan Suture regions (Fig. 1a; Pang et al., 2013b; Zarrinkoub et al., 2010). The rather slow extension rate in northeastern Iran did not cause large-scale, upper mantle melting (e.g., McKenzie and Bickle, 1988; Pang et al., 2012), which is consistent with the lack of voluminous Eocene–Oligocene magmatism in most of northeastern Iran (Fig. 1a). The small amounts of magmatic rocks exposed in that region have distributions strictly controlled by the major faults (Fig. 1a; Saadat and Stern, 2012).

The extensional tectonic regime possibly lasted up until the Miocene–Quaternary (Chiu et al., 2013; Kaislaniemi et al., 2014; Pang et al., 2012; Saadat and Stern, 2012) and appears to be related to the third stage of partial melting in the lithospheric mantle beneath NE Iran. During this stage the spongy texture formed in some clinopyroxenes. The spongy rims display lower Al_2O_3 and Na_2O contents and Cr# values than the cores of the clinopyroxenes (Appendix Table 2S), which are similar to the compositional variations of the clinopyroxenes in the mantle xenoliths from the Western Qinling Orogenic Belt in central China (Su et al., 2011b). The authors have interpreted the spongy texture of the xenolithic clinopyroxene to be the result of decompression melting. The selective presence of the spongy texture in the spinel lherzolites and in the coarse-grained dunite implies that the extension was very limited in the Quaternary, only affecting the shallow lithospheric mantle. This conclusion is further supported by the rare Quaternary magmatism in the study area (Fig. 1b; Saadat and Stern, 2012).

6.4. Thermal structure of the lithosphere and their geological implications

Various geothermometers are available for common mafic–ultramafic rocks. Among them, the two-pyroxene thermometer of Wells (1977) is commonly used and is believed to give reliable estimates for both mantle lherzolite and pyroxenite (e.g., Yamamoto et al., 2012; Ying et al., 2013; Zhang et al., 2010a). We also employed several other geothermometers (Table 1) to estimate the equilibrium temperatures of the studied xenoliths. However, the mineral chemical data for the fine grains surrounding the porphyroclasts and the spongy rims of the clinopyroxenes were not used in the temperature calculation. The equilibrated textures (i.e., triple junctions) were used and the estimates from most models are well correlated with the results using Wells' thermometer, with the exception of the orthopyroxene-spinel-olivine thermometer of Sachtleben and Seck (1981), which yields relatively high temperatures (Table 1).

So far, no good geobarometer is available for spinel lherzolite and pyroxenite, although the single clinopyroxene barometer (Nimis and Taylor, 2000) is used in many studies. As Wu and Zhao (2011) stated, orthopyroxene associated with clinopyroxene, and containing >0.37 wt.% of Al_2O_3, should be used in the pressure estimation to

Table 1
Temperature and pressure estimates of the mantle xenoliths from Navai, Mashhad, NE Iran.

Sample	Rock type	T(W)	T(WB)	T(SS)	T(WS1)	T(WS2)	T(NT)	P(NT)
12-IR-ZS-84-32	Dunite						876	11.2
12-IR-ZS-84-39	Dunite						769	27.2
12-IR-ZS-84-25	Sp lherzolite	873	987	971	917	976	789	11.3
12-IR-ZS-84-17	Sp lherzolite	927	1035	953	903	953	876	15.4
12-IR-ZS-84-37	Sp lherzolite	960	1066	930	887	945	943	19.8
12-IR-ZS-84-15	Sp lherzolite	978	1042	996	928	963	951	13.8
12-IR-ZS-84-12	Sp lherzolite	954	1058	969	906	981	930	15.5
12-IR-ZS-84-16	Sp lherzolite	956	1060	949	903	960	928	15.8
12-IR-ZS-84-27	Sp lherzolite	955	1055	991	935	963	921	14.3
12-IR-ZS-84-9	Sp lherzolite	966	1064	1002	936	961	933	13.5
12-IR-ZS-84-35	Sp lherzolite	988	1074	1061	980	987	956	12.7
12-IR-ZS-84-29	Sp lherzolite	960	1054	1052	968	990	912	10.7
12-IR-ZS-84-14	Sp lherzolite	953	1055	1010	928	946	910	10.5
12-IR-ZS-84-13	Sp lherzolite	959	1039	1004	961	971	959	17.0
12-IR-ZS-84-19	Sp lherzolite	964	1048	1041	972	986	973	14.0
12-IR-ZS-84-30	Ol websterite	918	1008	1049	954	879	904	26.2
12-IR-ZS-84-38	Ol websterite	943	1030	1049	942	830	959	30.8
12-IR-ZS-84-33	Ol websterite	940	1017	1131	959	814	963	30.7
12-IR-ZS-84-22	Ol websterite	924	993				937	26.0
12-IR-ZS-84-24	Ol websterite	936	959				936	15.3
12-IR-ZS-84-10	Websterite	925	988				924	22.5
12-IR-ZS-84-26	Websterite	950	1004				979	28.9
12-IR-ZS-84-34	Websterite	911	986				900	25.1
12-IR-ZS-84-20	Websterite	916	967				940	26.2
12-IR-ZS-84-11	Websterite	933	1003				974	28.3
12-IR-ZS-84-28	Websterite	894	1009				963	26.6
12-IR-ZS-84-21	Websterite	940	972				966	12.8
12-IR-ZS-84-36	Websterite	907	978				897	23.5
12-IR-ZS-84-41	Websterite	933	1002				946	25.9
12-IR-ZS-84-42	Websterite	934	997				939	25.1
12-IR-ZS-84-31	Websterite	901	967				921	24.7
12-IR-ZS-84-23	Clinopyroxenite	899	964				941	33.4

Note: T(W), Wells (1977) Opx-Cpx; T(WB), Wood and Banno (1973) Opx-Cpx; T(SS), Sachtleben and Seck (1981) Opx-Sp-Ol; T(WS1), Witt-Eickschen and Seck (1991) Opx-Sp; T(WS2), Witt-Eickschen and Seck (1991) Opx; T(NT), Nimis and Taylor (2000) Single Cpx; P(NT), Nimis and Taylor (2000) Single Cpx.

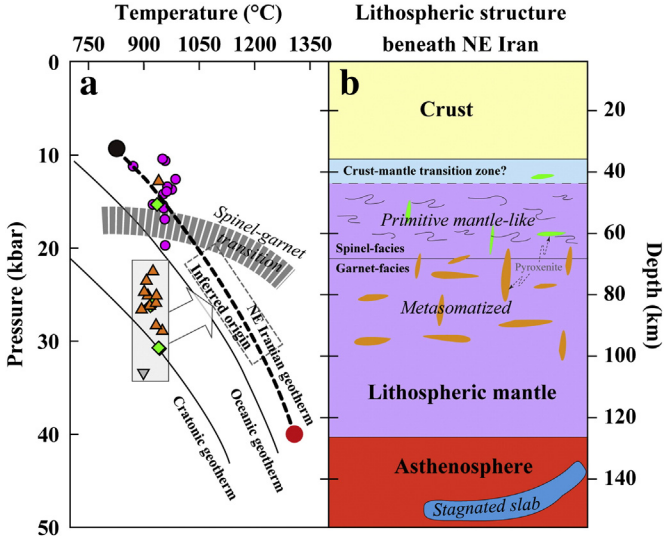

Fig. 12. (a) Temperature–pressure diagram of the NE Iranian mantle xenoliths. Temperature estimates from geothermometer by Wells (1977) are used. The field of inferred origin for the pyroxenite is based on the mineral chemistry discussed in the main text. The typical cratonic and oceanic geotherms are from Menzies and Chazot (1995). The black dot represents equilibrium temperature and pressure estimates of granulite xenoliths (Saadat and Stern, 2012) and the large red dot at 1300 °C and 125-km depth is from the tomographic model (Priestley et al., 2012). (b) Schematic illustration of the lithospheric structure beneath NE Iran. The Moho depth at ~40 km is from Manaman et al. (2011) and Amini et al. (2012). The lithosphere–asthenosphere boundary (LAB) at ~125 km is based on Manaman et al. (2011) and Priestley et al. (2012). The lithospheric mantle, composed largely of spinel and garnet bearing lherzolites, mixes with olivine websterite (green ribbons) and websterite (orange ribbons), respectively. See text for more detailed discussion.

avoid the significant propagation of analytical errors. All of the orthopyroxenes in this study have Al_2O_3 contents higher than 1 wt.% (Appendix Table 1S; Fig. 6), which make it possible to use the single clinopyroxene barometer for reference. The estimated pressures of all of the spinel lherzolites in this study, except for one (sample 12-IR-ZS-84-37), plot in spinel-facies peridotite field. The pyroxenites fall in a higher pressure field (Fig. 12a), which is consistent with the petrological and chemical inference that they have a garnet-facies peridotite protolith. Because these models match the other conclusions drawn from our data, the results estimated from Wells' thermometer and single clinopyroxene barometer are used for discussion hereafter.

The temperature estimates indicate that both the spinel lherzolites and the pyroxenites have equilibrated at temperatures of 900–1000 °C, which overlap the range calculated by Saadat and Stern (2012). The pressure estimates for the spinel lherzolites are in the range of 10.5–17 kbar, corresponding to a depth of 36–56 km (except for sample 12-IR-ZS-84-37 at 19.8 kbar and 64 km), while the pyroxenites are mostly in the pressure range of 22.5–33.4 kbar, corresponding to a depth of 72–105 km, with two samples (at 12.8 kbar and 43 km and 15.3 kbar and 50 km) falling in the spinel lherzolite range (Table 1; Fig. 12a). Similar higher pressure and lower temperature pyroxenite has been found in the lithospheric mantle at many locations worldwide (i.e., Beni Bousera; Frets et al., 2012).

A few of the lithospheric thermal conditions beneath the study area are also possible to evaluate. For instance, tomographic modeling gives a temperature estimate of 1300 °C at a depth of 125 km (Priestley et al., 2012). The granulites studied by Saadat and Stern (2012) yield ~850 °C equilibrium temperatures and ~9.8 kbar pressure. Based on all of these temperature and pressure estimates, the geothermal line can be broadly deciphered, as shown in Fig. 12a. Overall, the geotherm of the study

area is higher than that of cratonic and oceanic regions (Fig. 12a). However, tomographic imaging reveals a higher upper mantle velocity in the xenolith locality than in the adjacent Alborz Range, Sabzevar Zone, and even in Central Iran, where the low-velocity anomaly is widely observed (Amini et al., 2012). Low velocity anomalies in the upper mantle are usually an indication of a hot mantle (Amini et al., 2012; Maggi and Priestley, 2005; McKenzie and Priestley, 2008; Paul et al., 2010; Priestley et al., 2012). Thus, the Iranian Pateau has a relatively hot lithospheric mantle, and the lower temperature in the study area is probably due to low-temperature pyroxenites having an especially large presence in the garnet-facies mantle. This is further supported by the significant high-velocity anomaly in the Kopeh Dagh belt down to a depth of at least 120 km, which is interpreted to be the result of the relatively cold upper mantle structure (Manaman et al., 2011).

The lithospheric thickness has not been clearly defined in NE Iran. The pressure estimates in this study indicate that the lithosphere is at least ~105 km thick. Shear wave velocity models reveal that the lithosphere in NE Iran is <140 km thick, thinner than the Zagros belt (>225 km thick) and the South Caspian Basin (180–200 km thick) (McKenzie and Priestley, 2008; Priestley et al., 2012). The authors also find considerable lateral variations in the velocity at 125 km depth and suggest that the base of the lithosphere for the major part of the Iranian plateau is at 100–125 km. Therefore, in the xenolith locality, the lithospheric thickness can be assumed to be ~125 km (Fig. 12b).

The crustal thickness of the Iranian Plateau has been investigated by some geophysical surveys. In general, the Zagros belt has the thickest crust, up to 65 km, due to the Arabian–Eurasian continental collision (Maggi and Priestley, 2005; Molinaro et al., 2005; Paul et al., 2010), and the South Caspian basin has the thinnest crust, at ~33 km (Manaman et al., 2011; Paul et al., 2010). Gravity observations reveal that the crust beneath the mountain ranges of eastern Iran are 45–48 km thick, while in northern Iran, the crust beneath the Alborz Range is ~35 km thick (Dehghani and Makris, 1984). Moho maps derived using receiver functions (Radjaee et al., 2010) and waveform tomography studies (Manaman et al., 2011; Motaghi et al., 2012b) show a relatively thick crust (40–50 km) beneath NE Iran and ~42 km thick beneath the xenolith locality. The granulite points to a crust thicker than 34 km (Fig. 12a; Saadat and Stern, 2012), which is consistent with the geophysical observations. Three mantle xenoliths, however, provide depth constraints on the order of 36–38 km, possibly indicating that the crust–mantle boundary is at that depth (Fig. 12a). This inconsistency might be the result of uncertainty in the pressure estimates. Alternatively, a ~6-km-thick transition zone between the crust and mantle may exist in the lithosphere (Fig. 12b).

In many studies, seismic velocity anomalies have been detected at varying depths below the Iranian Plateau. It is worth noting that both the velocity anomaly amplitudes and geometries are well recovered at 75 km depth throughout most of the region (Priestley et al., 2012). This signature is related to either the spinel-garnet transition or the presence of pyroxenites (Fig. 12b). We prefer the latter explanation because the relatively 'cold' pyroxenite, unlike the mineral phase transition, plays a significant role in changing seismic velocity in the study area. Our argument is compatible with the Bouguer anomaly in the eastern Kopeh Dagh (Motaghi et al., 2012b), since pyroxenite is denser than peridotite. Some authors suggested that some of the late Cenozoic volcanism in eastern Iran originated from a garnet-facies mantle source (70–80 km) (e.g., Maggi and Priestley, 2005; Saadat and Stern, 2012; Walker et al., 2009). We suggest that the pyroxenites might be a major contributor (particularly of potassium via the consumption of alkali feldspar) to the mantle source of the potassic and ultra-potassic volcanic rocks, and that the alkali basalts similar in composition to the host rocks of xenoliths were derived from deeper mantle, most likely the asthenosphere. Regional analyses of seismology, gravity, and volcanism all suggest the presence of a thin, cold, metasomatized lithosphere beneath the NE Iranian Plateau relative to the Central Iran.

7. Concluding remarks

Petrological and mineral composition data of a variety of mantle xenoliths from NE Iran allow us to better understand the composition and structure of the lithospheric mantle in the region. The data suggest that the shallow part of the lithospheric mantle at depths of ~40–70 km is composed dominantly of deformed and primitive mantle-like spinel lherzolite. The deeper portion (~70–100 km) of the lithospheric mantle is characterized by the widespread presence of low-temperature pyroxenites, which we interpret as the products of mantle metasomatism by partial melts released from the stagnant slab in the asthenosphere. Multiple partial melting events within the lithospheric mantle are observed and interpreted to have resulted from the episodic albeit local extension in the region. The compositional and structural features revealed by our xenolith data are broadly consistent with independent lines of evidence from seismology, gravity and volcanism, while the deep processes that occurred in the lithospheric mantle are closely related to Arabian–Eurasian convergence involving the Tethyan subduction processes.

Supplementary data to this article can be found online at http://dx.doi.org/10.1016/j.lithos.2014.06.002.

Acknowledgements

We thank Hao-Yang Lee and Han-Yi Chiu for assistance in the fieldwork, Qian Mao and Yuguang Ma for assistance with the EPMA analyses, Zhaochu Hu for assistance with the LA-ICP-MS analyses, and Sanjeewa P.K. Malaviarachchi for reading an early version of this paper. We also thank Andrew Kerr (the editor), Adam Martin and an anonymous reviewer for very detailed and constructive comments that have helped improve the paper. Financial supports from the National Science Council, Taiwan, ROC and National Taiwan University, "Strategic Priority Research Program (B)" of the Chinese Academy of Sciences (Grant XDB03010800), Research Project on Iran Geodynamics from the State Key Laboratory of Lithospheric Evolution, National Natural Science Foundation of China (Grant41173011), and Hong Kong Scholars Program (No. XJ2012048) are gratefully acknowledged.

References

Alaminia, Z., Karimpour, M.H., Homam, S.M., Finger, F., 2013. The magmatic record in the Arghash region (northeast Iran) and tectonic implications. International Journal of Earth Sciences 102, 1603–1625.
Allen, M.B., Kheirkhah, M., Neill, I., Emami, M.H., McLeod, C.L., 2013. Generation of Arc and within-plate chemical signatures in collision zone magmatism: Quaternary lavas from Kurdistan Province, Iran. Journal of Petrology 54, 887–911.
Amini, S., Shomali, Z.H., Koyi, H., Roberts, R.G., 2012. Tomographic upper-mantle velocity structure beneath the Iranian Plateau. Tectonophysics 554–557, 42–49.
Anders, E., Grevesse, N., 1989. Abundances of the elements: Meteoritic and solar. Geochimica et Cosmochimica Acta 53, 197–214.
Asiabanha, A., Foden, J., 2012. Post-collisional transition from an extensional volcanosedimentary basin to a continental arc in the Alborz Ranges, N-Iran. Lithos 148, 98–111.
Chen, L., Liu, Y., Hu, Z., Gao, S., Zong, K., Chen, H., 2011. Accurate determinations of fifty-four major and trace elements in carbonate by LA-ICP-MS using normalization strategy of bulk components as 100%. Chemical Geology 284, 283–295.
Chiu, H.Y., Chung, S.L., Zarrinkoub, M.H., Mohammadi, S.S., Khatib, M.M., Iizuka, Y., 2013. Zircon U-Pb age constraints from Iran on the magmatic evolution related to Neotethyan subduction and Zagros orogeny. Lithos 162–163, 70–87.
Chung, S.L., Chu, M.F., Zhang, Y., Xie, Y., Lo, C.H., Lee, T.Y., Lan, C.Y., Li, X., Zhang, Q., Wang, Y., 2005. Tibetan tectonic evolution inferred from spatial and temporal variations in post-collisional magmatism. Earth-Science Reviews 68, 173–196.
Dargahi, S., Arvin, M., Pan, Y., Babaei, A., 2010. Petrogenesis of post-collisional A-type granitoids from the Urumieh-Dokhtar magmatic assemblage, Southwestern Kerman, Iran: Constraints on the Arabian–Eurasian continental collision. Lithos 115, 190–204.
Davies, J.H., von Blanckenburg, F., 1995. Slab breakoff: A model of lithosphere detachment and its test in the magmatism and deformation of collisional orogens. Earth and Planetary Science Letters 129, 85–102.
Dehghani, G.A., Makris, J., 1984. The gravity field and crustal structure of Iran. Neues Jahrbuch Geologie Paläontologie Abhanlungen 168, 215–229.
Frets, E., Tommasi, A., Garrido, C.J., Padrón-Navarta, J.A., Amri, I., Targuisti, K., 2012. Deformation processes and rheology of pyroxenites under lithospheric mantle conditions. Journal of Structural Geology 39, 138–157.
Gaul, O.F., Griffin, W.L., O'Reilly, S.Y., Pearson, N.J., 2000. Mapping olivine composition in the lithospheric mantle. Earth and Planetary Science Letters 182, 223–235.

Golonka, J., 2004. Plate tectonic evolution of the southern margin of Eurasia in the Mesozoic and Cenozoic. Tectonophysics 381, 235–273.
Gorring, M.L., Kay, S.M., 2000. Carbonatite metasomatized peridotite xenoliths from southern Patagonia: Implication for lithospheric processes and Neogene plateau magmatism. Contributions to Mineralogy and Petrology 140, 55–72.
Griffin, W.L., O'Reilly, S.Y., Ryan, C.G., 1999. The composition and origin of sub-continental lithospheric mantle. In: Fei, Y., Mysen, B.O. (Eds.), Mantle petrology: Field observations and high-pressure experimentation: A tribute to Francis R. (Joe) Boyd: In: Ber1tKa, C.M. (Ed.), The Geochemical Society Special Publication, Houston, pp. 13–45.
Hansen, L.N., Zhao, Y.H., Zimmerman, M.E., Kohlstedt, D.L., 2014. Protracted fabric evolution in olivine: Implications for the relationship among strain, crystallographic fabric, and seismic anisotropy. Earth and Planetary Science Letters 387, 157–168.
Hatzfeld, D., Molnar, P., 2010. Comparisons of the kinematics and deep structures of the Zagros and Himalaya and of the Iranian and Tibetan Plateaus and geodynamic implications. Reviews of Geophysics 48, RG2005. http://dx.doi.org/10.1029/2009RG000304.
Herzberg, C., 2011. Identification of source lithology in the Hawaiian and Canary Islands: Implications for origins. Journal of Petrology 52, 113–146.
Ionov, D.A., Dupuy, C., O'Reilly, S., Kopylova, M.G., Genshaft, Y.S., 1993. Carbonated peridotite xenoliths from Spitsbergen: Implications for trace element signature of mantle carbonate metasomatism. Earth and Planetary Science Letters 119, 283–294.
Jannessary, M.R., Melcher, F., Lodziak, J., Meisel, T.C., 2012. Review of platinum-group element distribution and mineralogy in chromitite ores from southern Iran. Ore Geology Reviews 48, 278–305.
Jimenez-Munt, I., Fernàndez, M., Saura, E., Verges, J., Garcia-Castellanos, D., 2012. 3-D lithospheric structure and regional/residual Bouguer anomalies in the Arabia-Eurasia collision (Iran). Geophysical Journal International 190, 1311–1324.
Kaislaniemi, L., van Hunen, J., Allen, M.B., Neill, I., 2014. Sublithospheric small-scale convection—A mechanism for collision zone magmatism. Geology 42, 291–294.
Kaviani, A., Hatzfeld, D., Paul, A., Tatar, M., Priestley, K., 2009. Shear-wave splitting, lithospheric anisotropy, and mantle deformation beneath the Arabia-Eurasia collision zone in Iran. Earth and Planetary Science Letters 286, 371–378.
Kay, R.W., Mahlburg Kay, S., 1993. Delamination and delamination magmatism. Tectonophysics 219, 177–189.
Kheirkhah, M., Neill, I., Allen, M.B., Ajdari, K., 2013. Small-volume melts of lithospheric mantle during continental collision: Late Cenozoic lavas of Mahabad, NW Iran. Journal of Asian Earth Sciences 74, 37–49.
Liotard, J.M., Dautria, J.M., Bosch, D., Condomines, M., Mehdizadeh, H., Ritz, J.F., 2008. Origin of the absarokite-banakite association of the Damavand volcano (Iran): Trace elements and Sr, Nd, Pb isotope constraints. International Journal of Earth Sciences 97, 89–102.
Liu, Y.S., Hu, Z.C., Gao, S., Günther, D., Xu, J., Gao, C.G., Chen, H.H., 2008. In situ analysis of major and trace elements of anhydrous minerals by LA-ICP-MS without applying an internal standard. Chemical Geology 257, 34–43.
Maggi, A., Priestley, K., 2005. Surface waveform tomography of the Turkish-Iranian plateau. Geophysical Journal International 160, 1068–1080.
Manaman, N.S., Shomali, H., 2010. Upper mantle S-velocity structure and Moho depth variations across Zagros belt, Arabian–Eurasian plate boundary. Physics of the Earth and Planetary Interiors 180, 92–103.
Manaman, N.S., Shomali, H., Koyi, H., 2011. New constraints on upper-mantle S-velocity structure and crustal thickness of Iranian plateau using partitioned waveform inversion. Geophysical Journal International 184, 247–267.
McKenzie, D.P., Bickle, M.J., 1988. The volume and composition of melt generated by extension of the lithosphere. Journal of Petrology 29, 627–679.
McKenzie, D., Priestley, K., 2008. The influence of lithospheric thickness variations on continental evolution. Lithos 102, 1–11.
McQuarrie, N., van Hinsbergen, D.J.J., 2013. Retrodeforming the Arabia–Eurasia collision zone: Age of collision versus magnitude of continental subduction. Geology 41, 315–318.
Menzies, M.A., Chazot, G., 1995. Fluid processes in diamond to spinel facies shallow mantle. Journal of Geodynamics 20, 387–415.
Mirnejad, H., Hassanzadeh, J., Cousens, B.L., Taylor, B.E., 2010. Geochemical evidence for deep mantle melting and lithospheric delamination as the origin of the inland Damavand volcanic rocks of northern Iran. Journal of Volcanology and Geothermal Research 198, 288–296.
Molinaro, M., Zeyen, H., Laurencin, X., 2005. Lithospheric structure beneath the southeastern Zagros Mountains, Iran: Recent slab break-off? Terra Nova 17, 1–6.
Motaghi, K., Tatar, M., Shomali, Z.H., Kaviani, A., Priestley, K., 2012a. High resolution image of uppermost mantle beneath NE Iran continental collision zone. Physics of the Earth and Planetary Interiors 208–209, 38–49.
Motaghi, K., Tatar, M., Priestley, K., 2012b. Crustal thickness variation across the northeast Iran continental collision zone from teleseismic converted waves. Journal of Seismology 16, 253–260.
Mottaghi, A.A., Rezapour, M., Korn, M., 2013. Ambient noise surface wave tomography of the Iranian Plateau. Geophysical Journal International 193, 452–462.
Ni, J., Barazangi, M., 1986. Seismotectonics of the Zagros continental collision zone and a comparison with the Himalayas. Journal of Geophysical Research 91, 8205–8218.
Nimis, P., Taylor, W.R., 2000. Single-clinopyroxene thermobarometry for garnet peridotites. Part I. Calibration and testing of a Cr-in-Cpx barometer and an enstatite-in-Cpx thermometer. Contributions to Mineralogy and Petrology 139, 541–554.
Niu, Y.L., 2005. Generation and evolution of basaltic magmas: Some basic concepts and a new view on the origin of Mesozoic-Cenozoic basaltic volcanism in eastern China. Geological Journal of China Universities 11, 9–46.
Omrani, J., Agard, P., Whitechurch, H., Benoit, M., Prouteau, G., Jolivet, L., 2008. Arc-magmatism and subduction history beneath the Zagros Mountains, Iran: A new report of adakites and geodynamic consequences. Lithos 106, 380–398.
Pang, K.N., Chung, S.L., Zarrinkoub, M.H., Mohammadi, S.S., Yang, H.M., Chu, C.H., Lee, H.Y., Lo, C.H., 2012. Age, geochemical characteristics and petrogenesis of Late Cenozoic intraplate alkali basalts in the Lut-Sistan region, eastern Iran. Chemical Geology 306–307, 40–53.
Pang, K.N., Chung, S.L., Zarrinkoub, M.H., Lin, Y.C., Lee, H.Y., Lo, C.H., Khatib, M.M., 2013a. Iranian ultrapotassic volcanism at ~11 Ma signifies the initiation of post-collisional magmatism in the Arabia-Eurasia collision zone. Terra Nova 25, 405–413.
Pang, K.N., Chung, S.L., Zarrinkoub, M.H., Khatib, M.M., Mohammadi, S.S., Chiu, H.Y., Chu, C.H., Lee, H.Y., Lo, C.H., 2013b. Eocene-Oligocene post-collisional magmatism in the Lut-Sistan region, eastern Iran: Magma genesis and tectonic implications. Lithos 180–181, 234–251.
Paul, A., Hatzfeld, D., Kaviani, A., Tatar, M., Pequegnat, C., 2010. Seismic imaging of the lithospheric structure of the Zagros mountain belt (Iran). Geological Society, London, Special Publications 330, 5–18.
Priestley, K., McKenzie, D., Barron, J., Tatar, M., Debayle, E., 2012. The Zagros core: Deformation of the continental lithospheric mantle. Geochemistry, Geophysics, Geosystems 13, Q11014.
Radjaee, A., Rham, D., Mokhtari, M., Tatar, M., Priestley, K., Hatzfeld, D., 2010. Variation of Moho depth in the central part of the Alborz mountains, northern Iran. Geophysical Journal International 181, 173–184.
Rudnick, R.L., McDonough, W.F., Chappell, B.W., 1993. Carbonatite metasomatism in the northern Tanzanian mantle: Petrographic and geochemical characteristics. Earth and Planetary Science Letters 114, 463–475.
Rudnick, R.L., Gao, S., Ling, W.L., Liu, Y.S., McDonough, W.F., 2004. Petrology and geochemistry of spinel peridotite xenoliths from Hannuoba and Qixia, North China Craton. Lithos 77, 609–637.
Saadat, S., Stern, C.R., 2012. Petrochemistry of a xenolith-bearing Neogene alkali olivine basalt from northeastern Iran. Journal of Volcanology and Geothermal Research 225–226, 13–29.
Sachtleben, T.H., Seck, H.A., 1981. Chemical control of Al-solubility in orthopyroxene and its implications on pyroxene geothermometry. Contributions to Mineralogy and Petrology 78, 157–165.
Şengör, A.M.C., Natal'in, B.A., 1996. Paleotectonics of Asia: Fragments of a synthesis. In: Yin, A., Harrison, M. (Eds.), The tectonic evolution of Asia. Cambridge University Press, Cambridge, pp. 486–640.
Şengör, A.M.C., Altlner, D., Cin, A., Ustaomer, T., Hsu, K.J., 1988. Origin and assembly of the Tethyside orogenic collage at the expense of Gondwana land. In: Audley-Charles, M.G., Hallam, A.E. (Eds.), Gondwana and Tethys. Geological Society of London Special Publication. Blackwell, Oxford, pp. 119–181.
Shafiei, B., Haschke, M., Shahabpour, J., 2009. Recycling of orogenic arc crust triggers porphyry Cu mineralization in Kerman Cenozoic arc rocks, southeastern Iran. Mineralium Deposita 44, 265–283.
Sobolev, A.V., Hofmann, A.W., Sobolev, S.V., Nikogosian, I.K., 2005. An olivine-free mantle source of Hawaiian shield basalts. Nature 434, 590–597.
Su, B.X., Zhang, H.F., Sakyi, P.A., Qin, K.Z., Liu, P.P., Ying, J.F., Tang, Y.J., Malaviarachchi, S.P.K., Xiao, Y., Zhao, X.M., Mao, Q., Ma, Y.G., 2010. Formation of melt pockets in mantle peridotite xenoliths from the Western Qinling (Central China): Partial melting and metasomatism. Journal of Earth Science 21, 641–668.
Su, B.X., Zhang, H.F., Tang, Y.J., Chisonga, B., Qin, K.Z., Ying, J.F., Sayki, P.A., 2011a. Geochemical syntheses among the cratonic, off-cratonic and orogenic garnet peridotites and their tectonic implications. International Journal of Earth Sciences 100, 695–715.
Su, B.X., Zhang, H.F., Sakyi, P.A., Yang, Y.H., Ying, J.F., Tang, Y.J., Qin, K.Z., Xiao, Y., Zhao, X.M., Mao, Q., Ma, Y.G., 2011b. The origin of spongy texture of mantle xenolith minerals from the Western Qinling, Central China. Contributions to Mineralogy and Petrology 161, 465–482.
Su, B.X., Zhang, H.F., Deloule, E., Sakyi, P.A., Xiao, Y., Tang, Y.J., Hu, Y., Ying, J.F., Liu, P.P., 2012. Extremely high Li and low δ^7Li signatures in the lithospheric mantle. Chemical Geology 292–293, 149–157.
Su, B.X., Zhang, H.F., Deloule, E., Vigier, N., Hu, Y., Tang, Y.J., Xiao, Y., Sakyi, P.A., 2014. Distinguishing silicate and carbonatite mantle metasomatism by using lithium and its isotopes. Chemical Geology 381, 67–77.
Sun, S.S., McDonough, W.F., 1989. Chemical and isotopic systematic of oceanic basalts: Implications for mantle composition and processes. In: Norry, M.J., Saunders, A.D. (Eds.), Magmatism in the ocean basins. Geological Society Special Publication, pp. 313–345.
Szabo, C.S., Bodnar, R.J., Sobolev, A.V., 1996. Metasomatism associated with subduction-related, volatile-rich silicate melt in the upper mantle beneath the Nograd-Gomor Volcanic Field, Northern Hungary/Southern Slovakia: Evidence for silicate melt inclusions. European Journal of Mineralogy 8, 881–899.
Verdel, C., Wernicke, B.P., Hassanzadeh, J., Guest, B., 2011. A Paleogene extensional arc flare-up in Iran. Tectonics 30. http://dx.doi.org/10.1029/2010TC002809 TC3008.
Walker, R.T., Gans, P., Allen, M.B., Jackson, J., Khatib, M., Marsh, N., Zarrinkoub, M., 2009. Late Cenozoic volcanism and rates of active faulting in eastern Iran. Geophysical Journal International 177, 783–805.
Walter, M.J., 2003. Melt extraction and compositional variability in mantle lithosphere. In: Carlson, R.W. (Ed.), The mantle and core. Vol 2. Carnegie Institution of Washington, Treatise on Geochemistry, Washington, DC, pp. 363–394.
Wells, P.R.A., 1977. Pyroxene thermometry in simple and complex systems. Contributions to Mineralogy and Petrology 62, 129–139.
Witt-Eickschen, E., Seck, H.A., 1991. Solubility of Ca and Al in orthopyroxene from spinel peridotite: An improved version of an empirical geothermometer. Contributions to Mineralogy and Petrology 106, 431–439.
Wood, B.J., Banno, S., 1973. Garnet-orthopyroxene relationships in simple and complex systems. Contributions to Mineralogy and Petrology 42, 109–124.
Woodland, A.B., Seitz, H.M., Yaxley, G.M., 2004. Varying behaviour of Li in metasomatised spinel peridotite xenoliths from western Victoria, Australia. Lithos 75, 55–66.

Wu, C.M., Zhao, G.C., 2011. The applicability of garnet-orthopyroxene geobarometry in mantle xenoliths. Lithos 125, 1–9.
Yamamoto, J., Nishimura, K., Ishibashi, H., Kagi, H., Arai, S., Prikhod'ko, V.S., 2012. Thermal structure beneath Far Eastern Russia inferred from geothermobarometric analyses of mantle xenoliths: Direct evidence for high geothermal gradient in backarc lithosphere. Tectonophysics 554–557, 74–82.
Ying, J.F., Zhang, H.F., Tang, Y.J., Su, B.X., Zhou, X.H., 2013. Diverse crustal components in pyroxenite xenoliths from Junan, Sulu orogenic belt: Implications for lithospheric modification invoked by continental subduction. Chemical Geology 356, 181–192.
Zanchetta, S., Berra, F., Zanchi, A., Bergomi, M., Caridroit, M., Nicora, A., Heidarzadeh, G., 2013. The record of the Late Palaeozoic active margin of the Palaeotethys in NE Iran: Constraints on the Cimmerian orogeny. Gondwana Research 24, 1237–1266.
Zarrinkoub, M.H., Chung, S.L., Chiu, H.Y., Mohammadi, S., Khatib, M., Lin, I.J., Oct. 4–8, 2010. Zircon U–Pb age and geochemical constraints from the northern Sistan suture zone on the Neotethyan magmatic and tectonic evolution in eastern Iran. Abst. to GSA Conference on "Tectonic Crossroads: Evolving Orogens in Eurasia–Africa–Arabia". Ankara, Turkey.
Zarrinkoub, M.H., Pang, K.N., Chung, S.L., Khatib, M.M., Mohammadi, S.S., Chiu, H.Y., Lee, H.Y., 2012. Zircon U-Pb age and geochemical constraints on the origin of the Birjand ophiolite, Sistan suture zone, eastern Iran. Lithos 154, 392–405.
Zhang, H.F., Nakamura, E., Kobayashi, K., Ying, J.F., Tang, Y.J., 2010a. Recycled crustal melt injection into lithospheric mantle: Implication from cumulative composite and pyroxenite xenoliths. International Journal of Earth Sciences 99, 1167–1186.
Zhang, H.F., Deloule, E., Tang, Y.J., Ying, J.F., 2010b. Melt/rock interaction in remains of refertilized Archean lithospheric mantle in Jiaodong Peninsula, North China Craton: Li isotopic evidence. Contributions to Mineralogy and Petrology 160, 261–277.
Zheng, J.P., O'Reilley, S.Y., Griffin, W.L., Lu, F.X., Zhang, M., 1998. Nature and evolution of Cenozoic lithospheric mantle beneath Shandong Peninsula, Sino-Korean Craton, eastern China. International Geology Review 40, 471–499.
Zindler, A., Hart, S.R., 1986. Chemical geodynamics. Annual Review of Earth and Planetary Sciences 14, 493–571.